Thesis for the degree of Doctor of Philosophy

Dynamics and Reactivity of Cu-species in Cu-CHA for NH_3-SCR

Joachim Dithmer Bjerregaard

Department of Physics
Chalmers University of Technology
Göteborg, Sweden 2025

Dynamics and Reactivity of Cu-species in Cu-CHA for NH_3-SCR
Joachim Dithmer Bjerregaard
ISBN 978-91-8103-291-8

Doktorsavhandlingar vid Chalmers tekniska högskola
Ny serie nr 5749
ISSN 0346-718X

Department of Physics
Chalmers University of Technology
SE-412 96 Gothenburg
Sweden
Telephone +46 31 772 1000

Cover: Illustration of the reaction mechanism for NH_3-SCR over Cu-CHA and the effect of SO_2

Printed at Chalmers Digitaltryck
Göteborg, Sweden 2025

Dynamics and Reactivity of Cu-species in Cu-CHA for NH_3-SCR

Joachim Dithmer Bjerregaard
Department of Physics
Chalmers University of Technology

Abstract

Ammonia assisted selective catalytic reduction (NH_3-SCR) is currently the preferred method for abatement of NO_x for lean burn engines. The copper exchanged chabazite is state-of-the-art catalyst for this reaction thanks to superior hydrothermal stability and good low-temperature activity. One challenge, however, is the sensitivity to sulfur compounds, present in the exhaust gas. Even small amounts of sulfur exposure can drastically deactivate the catalyst and shorten its operational lifetime. Therefore, it is critical to understand the mechanism behind the NH_3-SCR activity and sulfur poisoning.

During low-temperature NH_3-SCR conditions, Cu^{I} ions are solvated by NH_3, and present as $[Cu(NH_3)_2]^+$ complexes. A critical step in the reaction is O_2 adsorption, which requires the pairing of two $[Cu(NH_3)_2]^+$ complexes and leads to the formation of Cu^{II} ions in a peroxo complex $[Cu_2O_2(NH_3)_4]^{2+}$. In this thesis, various computational techniques and experiments are used to elucidate the pairing of $[Cu(NH_3)_2]^+$ and SO_2-deactivation of Cu-CHA.

A machine learning force field (ML-FF) is developed including long-range interactions. Trained on density functional theory (DFT) data, the ML-FF enables molecular dynamics (MD) simulations of large systems over extended timescales with high accuracy. The results show that the pairing of $[Cu(NH_3)_2]^+$ is promoted by increasing the Cu-loading and Al-content and that it is strongly influenced by counter-diffusion of nearby cations such as $[Cu(NH_3)_2]^+$ or $NH_4{}^+$.

DFT calculations are used to study the mechanism for SO_2 poisoning during low-temperature NH_3-SCR. The calculations suggest that SO_2 reacts with the peroxo complex $[Cu_2O_2(NH_3)_4]^{2+}$ forming NH_4HSO_4 species that accumulate inside the CHA cage. The accumulation destabilizes the pairing of $[Cu(NH_3)_2]^+$ and, thus, O_2 adsorption. Moreover, flow reactor experiments show that sulfation and regeneration depend critically on the temperature. Based on experimental data, a kinetic model is developed, which describes and rationalizes the dynamic behavior of SO_2 poisoning and regeneration.

The present work combines theoretical and experimental techniques to give a comprehensive understanding of the NH_3-SCR reaction over Cu-CHA, and the deactivation caused by SO_2 which is essential for guiding the development of more active and sulfur-resistant catalysts.

Keywords: Cu-CHA, NH_3-SCR, Sulfur Deactivation, DFT, Machine Learning Force Field, Kinetic Modelling

Publications

This thesis is based on the following appended papers:

I. On the Interpretation of H_2-TPR from Cu-CHA using First-Principles Calculations
J. D. Bjerregaard, J. Han, D. Creaser, L. Olsson, and H. Grönbeck
The Journal of Physical Chemistry C, **128** (2024), 4525-4534

II. Mechanism for SO_2 Poisoning of Cu-CHA during Low-Temperature NH_3-SCR
J. D. Bjerregaard, M. Votsmeier and H. Grönbeck
Journal of Catalysis, **417** (2023), 497-506

III. Effect of SO_2 and SO_3 Exposure to Cu-CHA on Surface Nitrate and N_2O Formation for NH_3-SCR
J. Han, J. D. Bjerregaard, H. Grönbeck, D. Creaser and L. Olsson
ACS Engineering Au, **4** (2024), 405-421

IV. Kinetic Modeling of Sulfur Poisoning and Regeneration Cycles on Cu-CHA during NH_3-SCR
J. D. Bjerregaard, R. Uglietti, H. Grönbeck and M. Votsmeier
In manuscript

V. Influence of Aluminium Distribution on the Diffusion Mechanisms and Pairing of $[Cu(NH_3)_2]^+$ Complexes in Cu-CHA
J. D. Bjerregaard, M. Votsmeier and H. Grönbeck
Nature Communications, **16** (2025), 603

VI. On the NH_3 Inhibition of Low-Temperature NH_3-SCR for NO Removal over Cu-CHA
J. D. Bjerregaard, V. A. C. Saltão, R. Uglietti, H. Grönbeck and M. Votsmeier
In manuscript

Publications not included in the thesis

On-the-fly Neural Network Based Kinetic Monte Carlo Simulations of NH_3-SCR over Cu-CHA
J. D. Bjerregaard, M. Votsmeier and H. Grönbeck
In manuscript

My contributions to the publications

Paper I
I performed all the calculations and programmed the micro-kinetic model. With exception of the experimental parts, I wrote the first draft of the paper, which was finalized together with my co-authors.

Paper II
I performed all the calculations. I wrote the first draft of the paper, which was finalized together with my co-authors.

Paper III
I performed all the calculations. I wrote the draft for the theoretical part of the manuscript. The manuscript was finalized by all co-authors

Paper VI
I designed and analysed the experiments and developed the kinetic model. I wrote the first draft of the manuscript, which was finalized together with my co-authors.

Paper V
I developed the force-field and performed all the calculations. I wrote the first draft of the manuscript, which was finalized together with my co-authors.

Paper VI
I designed and analysed the experiments and developed the kinetic model. I wrote the first draft of the manuscript, which was finalized together with my co-authors.

Contents

1
Introduction

Since the advent of industrialization, humans have emitted large quantities of greenhouse and toxic gases into the atmosphere, primarily due to the combustion of fossil fuels such as coal, oil, and natural gas for energy production, transportation, and industrial processes. Emissions of gases such as CO_2 and CH_4 contribute to the greenhouse effect, which, leads to rising temperatures globally.[1] Simultaneously, there has been an increase in pollutants like nitrogen oxides,NO_x (NO and NO_2), SO_2, CO, and particulate matter (PM), affecting the local air quality. In fact, 99 % of the world population today, breathes air that surpasses the guidelines with respect to pollutants set by the World Health Organization (WHO),[2] which cause premature deaths. To put it into perspective, air pollution is the second largest risk factor of death, just after high blood pressure and before tobacco.[3] Thus, there is a need to reduce air pollution. A major contributor to air pollution is NO_x, which is mainly emitted through combustion processes from petrol or diesel-powered vehicles and power plants. Biogenic sources also exist, such as those from lightning and volcanic activities, although they are not as significant as anthropogenic emissions.[4] In the EU, the road transport sector is the largest source of NO_x, accounting for 39 % of the total emissions[5] with the energy production and distribution sector being the second largest, emitting 16 %.[5] However, increasingly stricter legislation has contributed to large improvements in NO_x emissions during the last decades. The NO_x emissions from transport in the EU have decreased by 53 % with respect to the 1990-level,[5] which is largely attributed to the development of new catalytic aftertreatment systems for NO_x control.[6] Despite these improvements, there is a continuous need to improve catalytic techniques for NO_x abatement, due to the increasingly stringent regulations concerning emissions from combustion engines.

1.1 Heterogeneous Catalysis

A catalyst is a material that increases the rate of a reaction by providing a more favorable alternative reaction path.[7] In addition, a catalyst can enhance the selectivity, meaning that a higher fraction of the reactants is converted into the desired product. Catalysts are generally divided into homogeneous, enzymatic, and heterogeneous catalysts. In homogeneous catalysts, the reactants and products are in the same phase as the catalyst.[8] Enzymatic catalysts are enzymes used in biochemical reactions. In heterogeneous catalysis, which is the topic of this thesis, the reactant and products have a different phase from the catalyst. The catalyst is typically

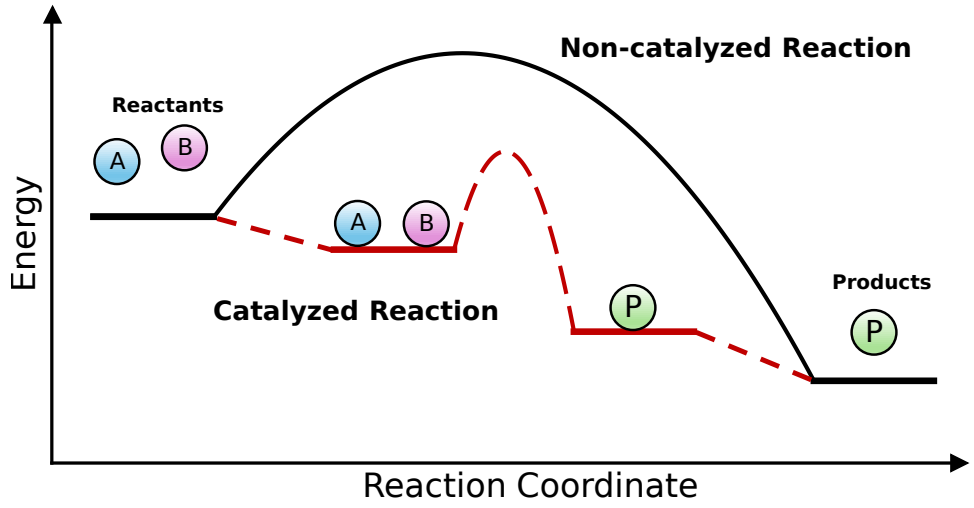

Figure 1.1: Potential energy diagram, for a catalyzed reaction and non-catalyzed reaction.

in solid phase while the reactants and products are in gas phase. The advantage of using heterogeneous catalysts is the ease of separating catalysts and products. A drawback is that they typically have lower selectivity compared to homogeneous catalysts.[8] Catalysts are a fundamental part of modern society, where it is estimated that 85 % of all chemical products are produced using catalysts.[9]

The influence of a catalyst on the potential energy landscape is illustrated in Figure 1.1. Two pathways from reactants to products are shown. Typically for surface reactions, the use of a catalyst introduces additional intermediates along the reaction coordinate, such as adsorption of reactants, diffusion of intermediates, surface reactions forming products, and desorption of products. Adsorbing the reactants on the surface brings them close together, facilitating their interaction, which is an important function of the catalyst. The catalyzed reaction has a lower activation barrier compared to the non-catalyzed reaction, resulting in an increased reaction rate as described by the Arrhenius equation.

$$r = Ae^{-E_a/k_BT} \tag{1.1}$$

Experimentally, the rate scales with the barrier, E_a. A is the pre-exponential factor, k_B is the Boltzmann constant and T is the temperature. The thermodynamics of the reaction is not affected by the presence of a catalyst.

Even though the catalyst is not consumed during the reaction, it may lose activity over time, due to deactivation. Examples of deactivation processes are poisoning of the active site by contaminants in the gas-feed, thermal degradation when the catalyst is operated at high temperature, or fouling, which is physical deposition onto the catalyst, such as carbon or coke.[10] Therefore, a catalyst should aim to achieve both high activity, high selectivity, and good stability.

1.2 NO_x Control

NO_x is formed during combustion in fuel engines and is associated with several negative health effects. Inhalation of NO_x can, for example, lead to respiratory and lung problems[2]. However, a large part of the harmful effects comes from reactions with other species in the atmosphere. Both NO and NO_2 are reactive molecules with short lifetimes of around 4 days.[4] NO_x is a precursor for the formation of tropospheric O_3 and can react with volatile organic compounds (VOC), which can lead to the formation of smog and acid rain.[11,12] Furthermore, NO_2 can react with OH radicals in the atmosphere, forming nitric acid[13] according to:

$$NO_2 + OH \longrightarrow HNO_3 \tag{R1}$$

Nitric acid HNO_3 is soluble in H_2O and contributes to acid rain, causing damage to the ecosystem.[12]

The use of a catalyst is the method of choice for NO_x control of fuel-powered vehicles. For gasoline cars, the three-way-catalyst (TWC) is used thanks to its ability to efficiently remove NO_x, CO, and hydrocarbon (HC) simultaneously. NO_x is reduced to N_2 and H_2O, while CO and HC are oxidised to CO_2 and H_2O. The TWC is typically based on Pt, Pd, and Rh nanoparticles supported on a metal oxide such as Al_2O_3.[14] Promoters in the form of metal oxides with high oxygen storage capacity, such as CeO_2 are also added. TWC has the limitation that it must be operating under stoichiometric conditions, which excludes the use of TWC in lean burn engines.
Lean burn engines, which operate with excess O_2, have gained increased attention thanks to their improved fuel economy and lower CO_2 emissions[15]. Instead of a TWC, the aftertreatment system typically used in lean burn engines contains two modules for the sequential removal of, on one hand, HC and CO, and on the other hand NO_x.[16] I) A diesel oxidation catalyst (DOC), usually based on platinum or palladium dispersed on a support, which oxidizes CO and HC[17]. II) An ammonia-assisted selective catalytic reduction (NH_3-SCR) catalyst for the removal of NO_x gases. The NH_3-SCR catalyst is placed downstream of the DOC. In NH_3-SCR, urea is heated, releasing NH_3, which is then dosed over the catalyst that reacts with NO_x to form N_2 and H_2O. The placement of a DOC in front of the NH_3-SCR catalyst increases the fraction of NO_2 in the exhaust, since a considerable amount of NO is oxidized to NO_2 over the DOC. This is beneficial since the reaction between NH_3, NO and NO_2 generally proceeds faster than that of NH_3 and NO.

1.3 Catalyst for NH_3-SCR

NH_3 can react with NO in presence of O_2 over the catalyst through the so-called, standard SCR reaction.

$$4\,NH_3 + 4\,NO + O_2 \longrightarrow 4\,N_2 + 6\,H_2O \tag{R2}$$

The stoichiometry between NH_3 and NO is one, and the presence of O_2 is required for the abstraction of the hydrogen atoms. In the presence of NO_2, the SCR reaction can proceed according to the so-called fast SCR reaction.

$$2\,NH_3 + NO + NO_2 \longrightarrow 2\,N_2 + 3\,H_2O \tag{R3}$$

N_2 and H_2O are the preferred products, however, side reactions can occur alongside the desired SCR reactions such as oxidation of NH_3 and NO with O_2. One particular important side reaction is the formation of N_2O.

$$2\,NH_3 + 2\,NO + O_2 \longrightarrow N_2 + N_2O + 3\,H_2O \tag{R4}$$

N_2O is a potent greenhouse gas that over a 100-year timespan, has a global warming potential 273 times greater than CO_2[18]. Therefore, the formation of N_2O should be minimized.

A catalyst suitable for NH_3-SCR should have redox properties to allow for O_2 adsorption and be able to adsorb and facilitate NO and NH_3 coupling. In addition, the catalyst must have a high stability, as it is exposed to harsh conditions in the aftertreatment system, including high temperatures and various exhaust contaminants that can lead to catalyst deactivation.
The two commercially available types of NH_3-SCR catalyst are vanadium-based and zeolite-based materials.[19] Vanadium is typically supported on TiO_2 and is characterized by a high activity in the medium temperature range and excellent SO_2 resistance.[20] A promoter such as WO_3 is often added to prevent unwanted phase transitions in TiO_2 and to enhance the low-temperature activity.[21] One drawback of using vanadium-based catalysts is the formation of volatile VO_x species, which pose a health risk when released into the ambient environment.[22]

Zeolites are hydrated crystalline aluminum silicates, composed of tetrahedral TO_4 sites where T is Si or Al.[23] They consist of interconnected cages and channels with dimensions as small as 1 nm, which give a high size selectivity and some of its unique properties. Pure silicates (SiO_2) do not contain any charges as silicon is tetravalent. However, as Al is trivalent, it requires a balancing counterion, often a proton. The proton can be ion-exchanged with a range of metals, such as Cu, Fe, Pd, and Pt, which are crucial for catalytic activity.[24] For NH_3-SCR Cu or Fe exchanged zeolites are typically used. For use in diesel-powered vehicles, Cu is preferred thanks to a good low-temperature activity and a good hydrothermal stability.[19] The different shapes and sizes of the zeolite framework give rise to many types. To date, there have been identified 255 zeolites as documented by the International Zeolite Association (IZA).[25] Each zeolite framework is assigned a 3-letter combination, with BEA and CHA being two with a high activity for NH_3-SCR.
BEA is classified as a large-pore-size zeolite with the largest ring consisting of 12 Si atoms. Cu-BEA has shown good tolerance against sulfur, however, it suffers from thermal degradation and hydrocarbon poisoning, which currently makes CHA the preferred choice for NH_3–SCR.[26–28] Chabazite, which is classified as a small-pore-size zeolite, consists of two cages, a small cage made up of four- and six-membered rings and a large cage, consisting of four- six- and eight-membered rings,

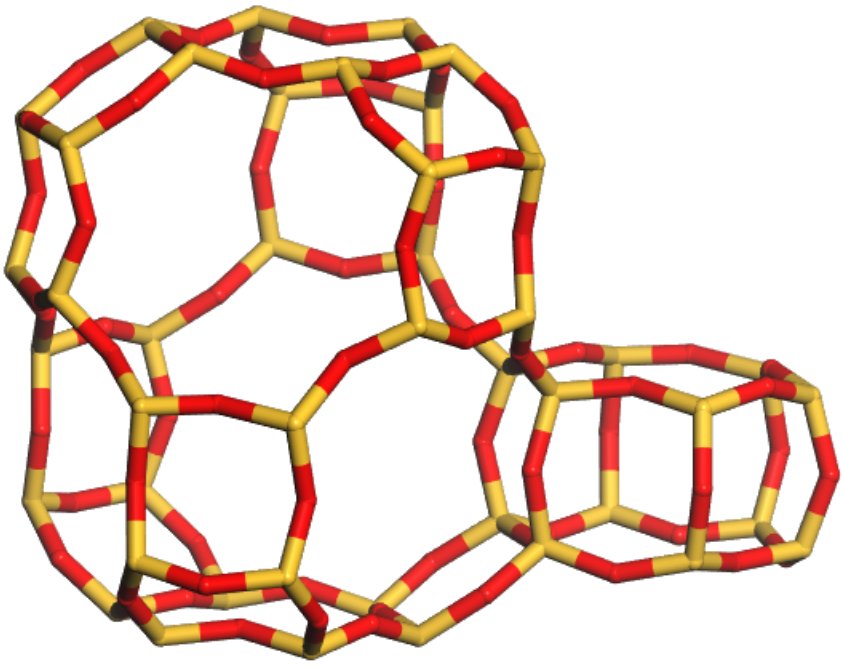

Figure 1.2: The two cages that make up the Chabazite structure. Atomic color codes: Si (yellow) and O (red).

shown in Figure 1.2. Cu exchanged chabazite (Cu-CHA) zeolites are known to have good hydrothermal stability,[29] with a good low-temperature activity to the SCR-reaction[30] and is the catalyst studied in this thesis.
The low-temperature NH_3-SCR mechanism over Cu-CHA has been extensively studied in recent years.[31–33] The reaction proceeds over NH_3 solvated copper complexes such as $[Cu(NH_3)_2]^+$. $[Cu(NH_3)_2]^+$ are mobile complexes that can diffuse between the CHA-cages and if two complexes are paired in the same cage, they can adsorb O_2 forming a peroxo complex $[Cu_2O_2(NH_3)_4]^{2+}$. NH_3 and NO can couple over the complex forming HONO and H_2NNO, which are decomposed to N_2 and H_2O. The NO-NH_3 coupling[32,33] reduces Cu^{II} back to $[Cu(NH_3)_2]^+$. The reaction is a redox-cycle where Cu changes between oxidation states +1 and +2. At higher temperatures NH_3 desorbs, forming framework-bound Cu ions. This give rise to a non-monotonic trend for the NO conversion as a function of temperature, where a minimum at around 350 °C is observed. This behavior suggests that two different mechanisms dominate at low and high temperatures.[34]

1.4 Catalyst Deactivation

Over time, the catalyst becomes deactivated, which impacts the activity and lifetime. The deactivation of a catalyst is closely related to the chemicals and temperature to which the catalyst is exposed. Exhaust gas contains various contaminants derived from the engine and fuel additives, that may deactivate Cu-CHA.[35] Simultaneously the temperature can reach up to 500 °C, which may accelerate the rate of deactivation. Furthermore, when exposed to H_2O at high temperatures, site re-

location, dealumination, and breakdown of the pore structure may occur, known as hydrothermal deactivation.[36]
Possible contaminants include phosphorus, alkali metals, and hydrocarbons, with sulfur being the most extensively investigated.[37–40] Sulfur is mainly in the form of SO_2 in the exhaust gas. However, as the DOC is placed upstream of the NH_3-SCR catalyst in the aftertreatment system, a part of SO_2 is oxidized to SO_3. Both SO_2 and SO_3 can cause significant deactivation of the catalyst over time.[37,38]
Cu-CHA is generally prone to sulfur deactivation compared to large pore size zeolite[28] and Fe-based zeolites.[41] Even small amounts of sulfur can accumulate in the zeolite and lead to substantial deactivation.[37] The exposure of the catalyst to sulfur might lead to the formation of sulfuric acid, ammonium (bi)sulfate, and Cu-sulfates.[40] A large part of the sulfur-induced deactivation can be regenerated by increasing the temperature to 500 °C, which is done periodically during operation, extending the lifetime of the catalyst.
However, some of the strongly bound sulfur remain in the zeolite and are not removed during the regeneration, resulting in a loss of activity over time.[38] The poisoning mechanism with sulfur is a complex process and depends on numerous factors, such as gas composition (O_2, H_2O, NO and NH_3), and temperature. There are some promising ways to limit sulfur deactivation by, for example, constructing a core-shell structure of cerium zink oxide around the zeolite.[42] However, these methods are in the early stage of development.

1.5 Objectives

The objective of the thesis is to investigate NH_3-SCR over a Cu-CHA zeolite with a focus on sulfur deactivation. This is done using a combination of theoretical and experimental techniques to gain a comprehensive understanding of the mechanisms behind these processes.

Cu-CHA is a dynamic system, where the state of Cu changes depending on temperature and gas composition.[43] Several experimental techniques exist that quantify the different Cu sites, where temperature-programmed reduction with hydrogen (H_2-TPR) is one example, which is studied in **Paper 1**. However the assignment of the peaks to atomic structures in Cu-CHA is ambiguous. In **Paper I**, a new method is developed to interpret H_2-TPR profiles, using density functional theory (DFT) based microkinetic modelling. In this approach, H_2 reactions over Cu species are investigated by DFT, which are used to simulate H_2-TPR profiles. In addition, H_2-TPR experiments are carried out to support our findings.

Paper II, **Paper III** and **Paper IV** focus on the sulfur poisoning. In **Paper II**, a detailed reaction mechanism is proposed for the deactivation of the low-temperature NH_3-SCR by SO_2. A thermodynamic analysis is carried out to investigate the most stable sulfur species at reaction conditions. As sulfur is proposed to limit the mobility of NH_3 solvated Cu species, constrained ab initio molecular dynamic simulation is performed to investigate the free energy barriers. In **Paper III** sulfur poisoning with both SO_2 and SO_3 at high temperatures and its effect on ammonium nitrate

and N_2O formation is investigated. DFT calculations for sulfur interaction with Cu complexes are performed to facilitate the interpretation of the experimental results. In **Paper IV**, a phenomenological kinetic model is constructed, which is constructed by parameter fitting to reactor-based experiments. To achieve this, repeated cycles of sulfation and thermal regeneration are performed to investigate the influence of different temperatures and gas compositions, for which the model can reproduce.

In **Paper V**, a machine learning force-field (ML-FF) is constructed that is trained using DFT data. The ML-FF is used to investigate the mobility and pairing of $[Cu(NH_3)_2]^+$ complexes in Cu-CHA. Molecular dynamic simulations for systems with thousands of atoms for nanoseconds are performed to investigate the effect of Si/Al ratio, Cu loading, counter ion, and Al distribution. MD simulation using metadynamics is performed to investigate the diffusion between zeolite cages and the collective effect between the ions.

In **Paper VI**, NH_3 blocking is investigated using a combined experimental and modeling approach. Transient response methods are performed to investigate the effect of NH_3 on the reduction of Cu^{II} species. A kinetic model including an NH_3 blocking step is developed to support and rationalize the experimental findings.

The thesis, which is partly based on my licentiate thesis,[44] contains seven chapters. In Chapter one, an introduction to the topic is given. In Chapter two, the electronic energy obtained from both density functional theory and machine learning force-fields is discussed. Chapter three introduces methods for simulating the system at elevated pressures and temperatures, such as molecular dynamics. Chapter four discusses how the system can be modeled using the mean-field approximation. Chapters five and six present an overview of the results obtained and Chapter seven presents the conclusions and outlook.

2

Electronic Energy

The knowledge about the electronic energy as a function of nuclear coordinates is fundamental to the study of chemical reactions, since it allows the identification of stable structures and transition states along reaction pathways. The electronic energy can be calculated by solving the Schrödinger equation using, for example, density functional theory (DFT) calculations. However, this is computationally expensive. An alternative approach is machine learning force-fields where the energy is parameterized using neural networks. This allows simulations of larger systems and extended simulation times. This chapter will introduce both of these methods.

2.1 The Schrödinger Equation

The time-independent Schrödinger equation is given by:

$$\hat{H}\psi = E\psi \tag{2.1}$$

$\hat{H}$ is the Hamiltonian operator, ψ is the wavefunction and E is the energy. The Hamiltonian can be written with operators for the potential and kinetic energies of the electrons and nuclei. It is convenient to write the Schrödinger equation in atomic units (au), which is defined as $m_e = e = \hbar = \frac{1}{4\pi\epsilon_0} = 1$.

$$\begin{aligned}\hat{H} = &- \sum_{A}^{nuclei} \frac{1}{2M_n}\nabla_n^2 - \sum_{i}^{elec} \frac{1}{2}\nabla_e^2 - \sum_{A}^{nuclei}\sum_{i}^{elec} \frac{Z_A}{R_A - r_i} \\ &+ \sum_{i}^{elec}\sum_{j>i}^{elec} \frac{1}{r_i - r_j} + \sum_{A}^{nuclei}\sum_{B>A}^{nuclei} \frac{Z_a Z_b}{|R_A - R_B|}\end{aligned} \tag{2.2}$$

The first two terms are the kinetic energy of the nuclei and electrons, respectively. The last three terms are the Coloumb interaction between nucleus-electron, electron-electron, and nucleus-nucleus, respectively. A first step when solving the Schrödinger equation is generally the Born-Oppenheimer approximation, allowing us to treat the wavefunctions of the nuclei and electrons separately. This approximation is based on the fact that the nuclei have a high mass compared to electrons, meaning that the nuclei can be seen as static relative to the motion of the electrons.

2.2 Hartree Fock Approximation

The Schrödinger equation (2.1) can only be solved analytically for one electron systems such as $H_2{}^+$. Thus, for the majority of chemical problems, the solution needs

to be approximated using numerical methods. One of the first successful approaches developed to solve the Schrödinger equation and the starting point for many other methods is the Hartree-Fock (HF) approximation.[45,46] In HF, the one-electron orbitals are arranged in a Slater determinant. The Slater determinant satisfies the Pauli principle, which states that the total electronic wavefunction must be antisymmetric, meaning that the wavefunction must change sign when interchanging two electron coordinates. The HF energy is given by:

$$E_{HF} = \sum_{i=1}^{N_{elec}} h_i + \frac{1}{2} \sum_{i=j}^{N_{elec}} \sum_{j=1}^{N_{elec}} (J_{ij} - K_{ij}) + V_{nn} \tag{2.3}$$

h_i is the energy given by the one-electron kinetic energy operator.

$$h_i = \langle \phi_i(1) | - \frac{1}{2}\nabla_i^2 - \sum_{A}^{N_{nuclei}} \frac{Z_A}{|R_A - r_i|} | \phi_i(1) \rangle \tag{2.4}$$

J_{ij} is the Coulomb integral and K_{ij} is the exchange integral. J_{ij} and K_{ij} are given by

$$J_{ij} = \langle \phi_i(1)\phi_j(2) | \frac{1}{|r_1 - r_2|} | \phi_i(1)\phi_j(2) \rangle \tag{2.5}$$

$$K_{ij} = \langle \phi_i(1)\phi_j(2) | \frac{1}{|r_1 - r_2|} | \phi_j(1)\phi_i(2) \rangle \tag{2.6}$$

V_{nn} is the nuclear repulsion. HF does not contain the full electron correlation as the many-body wavefunction is described by a single Slater determinant. The electron-electron repulsion is instead included in an average fashion, which can result in a poorly described ground state. On the other hand, HF contains the exact exchange energy, which means that electron self-interaction is absent. HF is the starting point of quantum chemical calculations such as coupled cluster (CC) and Møller–Plesset (MP).

2.3 Density Functional Theory Calculations

In 1964, Hohenberg and Kohn proposed two theorems that form the basis for DFT methods used today.[47] The first theorem states that the external potential V_{ext} is a unique functional of the electron density, ρ, which means that the ground state is also a unique functional of the electron density. The second theorem states that the ground state energy is a unique functional of the electron density. The clear advantage of using the electron density, ρ compared to wavefunction-based approaches is that the electron density, in principle, has the same number of variables independent of the size of the system. However, the functional connecting the energy and electron density is unknown.

Attempts at solving the ground state energy based only on the electron density give poor accuracy, with one reason being the difficulty in describing the kinetic energy. A solution is the introduction of Kohn-Sham orbitals,[48] used in modern DFT calculations. Within the Kohn–Sham formalism, the DFT total energy can be expressed as

$$E_{DFT}(\rho) = T_S(\rho) + E_{ne}(\rho) + J(\rho) + E_{xc}(\rho) \tag{2.7}$$

$T_S(\rho)$ is the kinetic energy expressed by single-electron orbitals for non-interaction electrons, where the wavefunction is constructed from a single Slater determinant similar to HF.

$$T_S(\rho) = \sum_{i=1}^{N_{elec}} \langle \phi_i | -\frac{1}{2}\nabla^2 | \phi_i \rangle \tag{2.8}$$

$E_{ne}(\rho)$ is the interaction between the nucleus and electrons, $J(\rho)$ is the electron-electron repulsion. For the first three terms, there are exact solutions available. However, for the exchange-correlation energy $E_{xc}(\rho)$, an approximation is needed. The choice of $E_{xc}(\rho)$ is crucial for the accuracy of DFT calculations and has led to the development of a wide range of exchange-correlation functionals.

2.3.1 Exchange Correlation Functionals

$E_{xc}(\rho)$ can be written as the sum of the exchange energy $E_x(\rho)$ and correlation energy $E_c(\rho)$. A simple approximation is the local density approximation (LDA)[47] where the electron density is treated locally as a uniform electron gas. Here the exchange energy is given as

$$E_x^{LDA}(\rho) = -\frac{3}{4}\left(\frac{3}{\pi}\right)^{1/3} \int \rho^{4/3}(r) dr \tag{2.9}$$

The correlation energy, E_c^{LDA} can be calculated with high accuracy based on quantum Monte Carlo simulations.[49] The approximation of a uniform electron gas fails in cases where the electron density does not vary slowly.
Improvements to LDA are possible by making the exchange-correlation depend on not only the electron density but also on the first derivate. One of these methods is known as generalized gradient approximation (GGA)[50] and the exchange energy can be written as

$$E_x^{GGA}(\rho, x) = \int \rho^{4/3} F(x) dr \tag{2.10}$$

$F(x)$ is an enhancement factor and x is the dimensionless density gradient. One well-known approximation within the GGA class is Perdew-Burke-Ernzerhof (PBE),[51] which is used in this thesis. Here, the enhancement factor is

$$F(x) = 1 + \kappa - \frac{\kappa}{1 + \mu x^2/\kappa} \tag{2.11}$$

κ and μ are constants. The correlation energy for GGA can be written as.[51]

$$E_c^{GGA}(\rho) = \int d^3 r \rho [\epsilon_C^{unif}(r_s, \zeta) + H(r_s, \zeta, t)] \tag{2.12}$$

r_s is the local Seitz radius, ζ is the relative spin polarization, ϵ_C^{unif} is the correlation energy per particle of a uniform gas and t is a dimensionless density gradient
A way to further improve the XC-approximation is to let the exchange-correlation energy depend on higher-order derivatives of the electron density, which includes the kinetic energy density and is called meta-GGA methods.[52]
Common for the LDA and GGA methods, is that they overdelocalise the electrons because the exchange-correlation term E_{xc}, does not cancel the self-interaction from

the electron-electron interaction (J_{ij}). This is especially important for the description of strongly correlated d- or f-electrons, which, for example, is the case for transition-metal oxides. In HF, this electron self-interaction is removed by the HF exchange. In hybrid methods, the self-interaction is reduced by adding a fraction of the HF exchange to the exchange-correlation. One example of a hybrid functional is B3LYP.[53,54]

$$E_{xc}^{B3LYP} = (1-a)E_x^{LSDA} + aH_x^{HF} + b\Delta E_x^{B88} + (1-c)E_c^{LSDA} + cE_c^{LYP} \tag{2.13}$$

Two different exchange energies are included, which are the exchange from HF, E_x^{HF} and B88, E_x^{B88}. The correlation part is the LYP functional E_c^{LYP}. The amount of exchange included is determined by the parameters a, b, and c, which are fitted to experimental data. Hybrid methods generally give more accurate results than GGA methods, for strongly correlated systems, however, there is an increasingly computational cost associated with the calculation of HF exchange.
Another way to reduce the issue with the self-interaction is augmenting DFT with a Hubbard U term,[55] which is computational inexpensive. Here, the strong on-site Columb interactions of the localized electrons are treated with an additional term, which stabilizes the localized orbitals with respect to delocalization. The choice of the U parameter is important and is method and material dependent. Typically different values of U are tested and compared with experiments or computational results. The U value can also be determined from first-principles[56].
Standard density functional theory does not contain dispersion forces and therefore cannot capture the attractive $1/R^6$ long-distance behavior between charge distributions that do not overlap. One solution is to augment GGA with a nonlocal correlation functional. An example of this is the van der Waals density (vdW-DF) functional proposed by Dion et al.[57] Dispersion forces can also be included using an empirical pairwise correction as suggested by Grimme[58] that accounts for the dispersion forces.

$$\Delta E_{disp} = -\sum_{n=6(8,10)} s_n \sum_{AB}^{atom} \frac{C_n^{AB}}{R_{AB}^n} f_{damp}(R_{AB}) \tag{2.14}$$

s_n is a scaling factors that depends on the functional applied, C_n^{AB} is a dispersion coefficient, for atom pair AB and R_{AB}^n is the distance between A and B for the n$^{\text{th}}$ order(n=6(8,10)). $f_{damp}(R_{AB})$ is the damping factor. Early models included only the 6$^{\text{th}}$ order term, but have been refined by including higher orders corrections.[52] This correction is referred to as DFT-D methods, where the DFT-D3 approach is used in this work.

2.3.2 Basis Sets and Pseudopotentials

When solving HF or DFT, they both require a basis set to represent the orbitals. This can either be done with local basis set functions, such as, Slater and Gaussian-type of orbitals centered at the atoms or in the form of plane waves. In this work, plane waves are used as they are the preferred choice for periodic systems, because they fulfill Bloch's theorem. Another advantage of plane wave is that they are

easier to converge.[59] Bloch's theorem states that the plane wave functions, at the same position in two different cells can be related by the lattice vector a.

$$\phi(r + a) = e^{ik \cdot r}\phi(r) \tag{2.15}$$

Plane waves are good at describing delocalized slowly varying electron densities, such as valence and conduction bands as the potential is rather smooth. However, this is not the case for core electrons that are localized with sharp peaks and many oscillations that require too many plane waves to describe. A solution to this problem is to treat the core electrons with an effective potential and only treat the valence electrons explicitly, which at the same time decreases the computational cost. This is possible since the core electrons are not involved in the formation and breaking of chemical bonds. These methods are known as pseudopotential methods and the Projector Augmented Wave (PAW)[60] proposed by Bloch is used in this thesis. In the PAW formalism, the all electron (AE) wave function can be obtained from the the pseudo (PS) wavefunction by:

$$|\Psi\rangle = |\tilde{\Psi}\rangle + \sum_i (|\phi_i\rangle - |\tilde{\phi}_i\rangle) \langle \tilde{p}_i | \tilde{\Psi}\rangle \tag{2.16}$$

$|\phi_i\rangle$ is the AE partial waves, $|\phi_i\rangle$ is the one PS partial wave and $\tilde{p}_i$ is the projector function. The advantages of the PAW approach is the computational efficiency of the plane waves combined with the accuracy provided by the augmentation.[59]

2.4 Analysis of Electronic Structure

Analysis of atomic charges is useful as it allows for studies of, for example, the oxidation state of Cu ions. A popular approach is the use of Bader charge analysis.[61,62] In Bader charge analysis, the charge density is partitioned into Bader volumes corresponding to each atom, which are separated by zero flux surfaces, where the charge density is a minimum perpendicular to the surface. Each Bader volume contains a single electron density maximum. Henkelman and co-workers, developed a method to partition the charge density into Bader volumes.[61,62] The method is grid-based and the partition algorithm follows the steepest ascent path along the charge density gradient until the maximum electron density is found. The total charge is then calculated by integrating over each Bader volume.

2.5 Parameterization of Energy

DFT is a powerful tool for calculating the electronic energy, however, DFT calculations have a high computational cost, which puts a limitation on what problems can be studied. As an alternative approach, the electronic energy can be calculated by parameterizing it as a function of nuclear coordinates, known as force-fields (FF).

2.5.1 Classical Force-Field

The FF energy can generally be written as different bonded and non-bonded terms contributing to the energy.[63]

$$E^{FF} = E_{str} + E_{bend} + E_{tors} + E_{vdw} + E_{el} + E_{cross} \tag{2.17}$$

E_{str} is the energy contribution from stretching of the bonds, E_{bend} describes the energy as a function of bending an angle between three atoms, E_{tors} is the torsion between four atoms. E_{vdw} and E_{el} describe the van der Waals and electrostatic contributions to the energy. Finally, E_{cross} represents the coupling between the different terms. The bonding terms ($E_{str} + E_{bend} + E_{tors}$) can be described by simple functions of distance, angle, and torsion, respectively. For the non-bonding terms, the van der Waals forces, E_{vdw} can be modeled using a Lennard-Jones potential while the electrostatic energy E_{el} can be modeled using a Coulomb law assuming point charge, however, higher-order forms may be included. The parameters for each term are typically fitted to experimental data or first-principle calculations. By parameterizing the electronic energy, and bypassing the DFT equations, it becomes possible to study systems with thousands of atoms. However, traditional FF, can be time-consuming to construct and require a detailed knowledge of how to model the system.[64] Furthermore, conventional force-fields such as AMBER[65] and UFF,[66] assume that the bonds between the atoms are predefined, and that bond formation and breaking do not occur, which limits its application.[67] More advanced bond-order force-fields like ReaxFF,[68] can model bond forming and breaking,[69] however, this adds more complexity to the force-field. In addition, they are often not sufficiently accurate for quantitative studies or are restricted to specific types of reactions.[67]

2.5.2 Machine Learning Force-Fields

Two of the main limitations of FF is their relatively poor accuracy and their inability to model chemical reactions compared to, first-principle methods such as DFT. With the use of machine learning it is possible to combine the accuracy of DFT with the low computational cost of FF, refereed to as machine learning force-fields (ML-FF).[67] ML-FF predicts energies and forces by means of machine learning such as a neural network, and do not consist of analytical expressions as is the case of traditional FFs. When trained on DFT calculations, ML-FF can achieve close to DFT accuracy at a computational cost, comparable to that of FF.
Many ML-FF algorithms rely on the assumption of chemical locality. In these cases, the total energy is a sum of the energies of the individual atoms.

$$E_{tot}^{ML-FF} = \sum_i E_i \tag{2.18}$$

The energy of for the individual atom, E_i is determined by the local atomic environment, within a cut-off radius r_{cut}, as illustrated for atom A in Figure 2.1(a). The local atomic environment is described by different descriptors. Two descriptors can be the distance r_{A-C} between atom A and C and the angle θ_{B-A-C} between atom B, A and C illustrated in Figure 2.1. These are simple examples, and in practice,

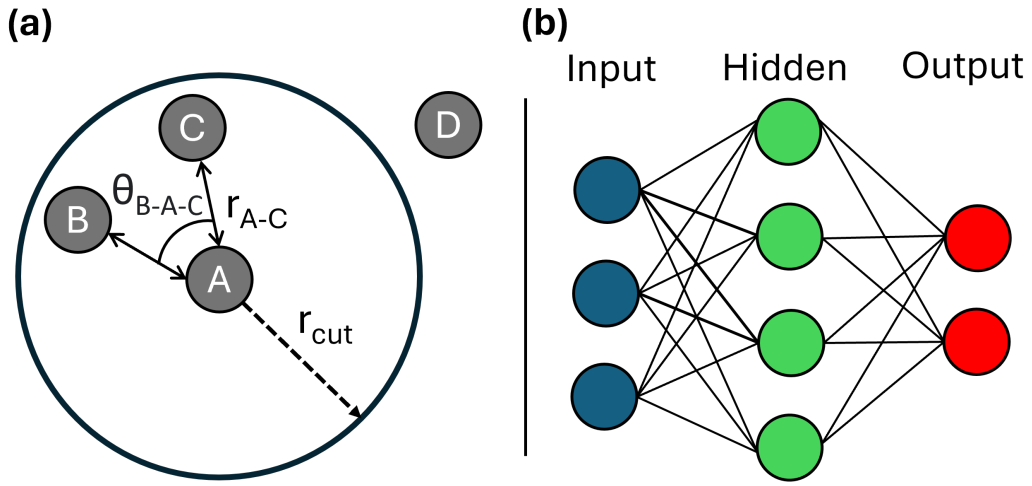

Figure 2.1: (a): The description of local atomic environment for atom A (b): A simple neural network showing three different layers, being the input layer, hidden layer and output layer.

more advanced descriptors such as symmetry functions or smooth overlap of atomic positions (SOAP) are often used. In Figure 2.1 the energy of atom A depends only on the atoms within its cut-off radius, which are atoms B and C. Atom D is outside the cut-off radius, and thus the energy of atoms A and D does not depend explicitly on each other, which can cause problems. The assumption of chemical locality reduces the computational cost as the interaction between all atoms does not have to be calculated. Furthermore, it makes it possible to extrapolate the ML-FF to larger systems after training. However, the drawback is the inability to describe long-range interactions, which can be important for, especially, charged systems.[70]

2.5.2.1 Long-range Interactions

Long-range interaction can be incorporated into a chemical locality based ML-FF by the use of charges in the form of spherical Gaussians. The ML-FF energy can in this way be augmented with the electrostatic energy. In this thesis, a recently developed method by Zhang et al[71] implemented in the Deep MD kit code[72] is used. The code was originally implemented with maximally localized Wannier functions. Here, however, atom-centered charges are used in this work instead. The energy can then be written as:

$$E_{tot}^{ML-FF} = E_{sr} + E_{G_t} \tag{2.19}$$

E_{sr} is the predicted energy from standard ML-FF using a radius cut-off. The introduced E_{G_t} term is the Gaussian electrostatic energy. Note that the Gaussian electrostatic energy E_{G_t} is subtracted from E_{sr} to avoid double counting. E_{G_t} is calculated in the Fourier space as

$$E_{G_t} = \frac{1}{2\pi V} \sum_{m \neq 0, |m| \leq L} \frac{\exp(-\pi^2 m^2/\beta^2)}{m^2} S(m)^2 \tag{2.20}$$

V is volume of the unit cell, L is the Fourier space cutoff and β is the spread parameter. $S(m)$ is the structure factor given by

$$S(m) = \sum_i q_i e^{-2\pi i m R_i} \tag{2.21}$$

q_i is the charge density of charge i, and R_i is the charged site. The particle-particle-particle-mesh (PPPM) algorithm is used to calculate the electrostatic energy. Note that it is not necessarily all atoms that are assigned a charge. The incorporation of the Gaussian electrostatic energy increases the computational cost by approximately a factor of 5 but is still superior in speed when compared to DFT calculations.[71] For the ML-FF developed in this thesis, an MD simulation can achieve a speed of 10 timesteps/s for a system consisting of $\approx$ 3500 atoms. In contrast, a single timestep of an AIMD simulation takes 150 s for a Cu-CHA system of 300 atoms.

2.5.2.2 Neural Network

The next step is to go from the descriptors presented in previous section to electronic energies and forces by the use of machine learning. Two commonly used algorithms for ML-FF are kernel method and neural network, with the latter used in this thesis.[73] A simple neural network is illustrated in Figure 2.1b, with input, hidden, and output as the layers. In practice, a neural network may have hundreds of neurons with several hidden layers depending on the complexity of the problem studied. The objective of the hidden layer is to transform the input (descriptors), into output (energy and forces). A single hidden layer can be expressed as

$$f(x) = \sum_{n=0}^{N} c_n \sigma(w_n x + b_n) \tag{2.22}$$

$f(x)$ corresponds to the output and x is the input, with N being the number of neurons, σ is the neuron activation function, which introduces non-linearity into the network. c_n, w_n and b_n are parameters fitted to a given set of training data.
Training the network is the process of fitting the parameters to a loss function.[72]

$$L(p_\epsilon, p_f, p_\xi) = p_\epsilon \Delta\epsilon^2 + \frac{p_f}{3N} \sum_i |\Delta F_i|^2 + \frac{p_\xi}{9} ||\Delta\xi||^2 \tag{2.23}$$

Δ is the difference between the force-field prediction and the training data, N is the number of atoms, ϵ is the energy per atom, F_i is the force on atom i, and ξ is the viral tensor (if included). p_ϵ, p_f and p_ξ are adjustable parameters, where $p_\in$ and p_f are increasing, and p_ξ decreasing during training. The training is a minimization problem of the loss function by tuning the parameters in the hidden layer(s).

3

Towards Elevated Pressure and Temperature

Electronic structure calculations introduced in the previous section, allows one to identify stable structures and transitions state, both of which are needed to describe chemical reactions. The calculated electronic energy, however, corresponds to zero kelvin and zero pressure, which does not represent experimental conditions. With statistical mechanics and thermodynamics, it is possible to add effects of temperature and pressure. An alternative approach is to solve Newton's equations of motion and simulate the system at finite temperatures and/or pressures via molecular dynamics (MD). When combined with ML-FF, MD simulation can be extended to approach microsecond regime. This chapter will discuss the process of adding the effects of temperature and pressure to the electronic energies calculated in the previous chapter.

3.1 Optimization

The search for a stable structure is a multidimensional optimization problem, where the nuclear coordinates are changed to minimize the energy of the system. The objective is to find a local minimum on the potential energy surface, hence, the gradient in all directions should be zero. Structural optimization always starts with an initial guess of the geometry, from which a stable structure should be found. The forces acting on the atoms, calculated using DFT or ML-FF, represent the gradient of the potential energy surface and can be used by different algorithms to search for a minimum.

A simple approach is to calculate the gradient and then take a step in the opposite direction, known as the steepest descent (SD) method.[52] Going in the opposite direction of the gradients, ensures that the energy will decrease, thus, it is guaranteed that a minimum will be found. However, SD tends to oscillate around the minimum and the convergence is slow.[52] A way to improve on the SD method, is to consider both the gradient and the gradient from the previous step in the optimization procedure. By doing so, the step is not taken against the gradient but along a line conjugate to the previous step, which ensures faster convergence than the SD method. This method is called conjugate gradient[52] and is the method used in this thesis. Note that the optimization algorithms only ensure that the structure converges to a local minimum, thus, it might not correspond to a stable structure. This is especially challenging for species in Cu-CHA, as the potential energy landscape

is flat. This issue has been tackled by using ab initio molecular dynamics (AIMD) to sample the potential energy landscape. Structures are then extracted along the trajectories and subsequently optimized, after which, the structure with the lowest energy is selected.

3.2 Transition State Search

Chemical reactions typically involve some kind of energy barrier that has to be passed to form the final products. The molecules follow the minimum energy path between the two minima with the highest point connecting them corresponding to the transition state, which is a first-order saddle point. Identifying first-order saddle points is typically more difficult than finding minima. For systems with a high degree of freedom, such as periodic systems, multi-structure interpolation methods like the climbing image nudge elastic band (CI-NEB) are generally used to identify transition states.[52] In NEB, a series of structures, called images, are interpolated between the initial and final state, which must be known. A spring is added that evenly distributes the images, along the reaction coordinate, mimicking an elastic band, hence the name. The images are optimized based on the perpendicular component of the true force, ensuring that the spring force does not interfere with the convergence of the images to the minimum energy path.[74] To find the transition state, the spring of the image with the highest energy is turned off, so the image experiences the true forces.[75] This image is, thereafter, converged to a first-order saddle point. A vibrational analysis, introduced in the next section, confirms if it is a true first-order saddle point.

3.3 Vibrational Analysis

At zero Kelvin, the molecules still vibrate and a correction to the electronic energy is added, to give the zero point energy (ZPE) electronic energy. Furthermore, vibrational analysis can be used to compute the vibrational entropy, which is necessary for estimating the Gibbs free energy. A common way to evaluate the vibrations is to approximate them as a harmonic oscillator. The vibrational frequencies can with this approximation be derived by a Taylor expansion involving the energy and nuclear coordinates. For a diatomic molecule, the only nuclear coordinate to consider is the bond length and the Taylor series becomes:[52]

$$E(R) = E(R_0) + \frac{dE}{dR}(R - R_0) + \frac{1}{2}\frac{d^2E}{dR^2}(R - R_0)^2 + \frac{1}{6}\frac{d^3E}{dR^3}(R - R_0)^3 + ... \quad (3.1)$$

The first term is the zero point of the energy, the second term vanishes since the structure vibrates around a minimum where the first derivate with respect to the nuclear coordinates is zero. The energy can, thus, be approximated as the lowest non-zero term, which is the second-order derivative.

$$E(R - R_0) \approx \frac{1}{2}\frac{d^2E}{dR^2}(R - R_0)^2 = \frac{1}{2}k(R - R_0)^2 \quad (3.2)$$

The second derivative is defined as the force constant k, which can be used to estimate the vibrational frequency v.

$$v = \frac{1}{2\pi}\sqrt{\frac{k}{\mu}} \tag{3.3}$$

μ is the reduced mass that for a diatomic molecule is $m_1 m_2/(m_1 + m_2)$.

3.4 Evaluation of Partition Functions

The structure and transition states discussed so far, correspond to structures at zero Kelvin at zero pressure. Statistical mechanics provide the connection between the properties of a single molecule and an ensemble of molecules at elevated temperatures and pressures. Essential for the connection is the partition function Q as several thermodynamic properties can be derived from the partition function[76] such as enthalpy H, entropy S, Helmholtz free energy F, and Gibbs free energy G.

$$H = U + PV = k_B T^2 \left(\frac{\partial \ln Q}{\partial T}\right)_V + k_B T V \left(\frac{\partial \ln Q}{\partial V}\right)_T \tag{3.4}$$

$$S = \frac{U - F}{T} = k_B T \left(\frac{\partial \ln Q}{\partial T}\right)_V + k_B \ln Q \tag{3.5}$$

$$F = -k_B T \ln Q \tag{3.6}$$

$$G = H - TS = k_B T V \left(\frac{\partial \ln Q}{\partial V}\right)_T - k_B T \ln Q \tag{3.7}$$

For a system consisting of N non-interaction, indistinguishable particles, the partition function Q is given by $Q = \frac{1}{N!} q^N$. q is the partition function for a single molecule, which is given by the sum of all possible quantum energy states, ϵ_i.

$$q = \sum_i^{\infty} e^{-\epsilon_i / k_B T} \tag{3.8}$$

The total partition function can be written as a product of terms involving the electronic, translation, rotation, and vibration degree of freedom.

$$q_{tot} = q_{trans} q_{rot} q_{vib} q_{elec} \tag{3.9}$$

The translation has three degrees of freedom, with the partition function depending on both the volume, V, and the mass, m.

$$q_{trans} = \left(\frac{2\pi m k_B T}{h^2}\right)^{3/2} V \tag{3.10}$$

Using the rigid-rotor approximation the rotational partition function for a polyatomic molecule can be calculated using the principal axes of inertia I_x and a symmetry factor σ.

$$q_{rot} = \frac{\sqrt{\pi}}{\sigma}\left(\frac{8\pi^2 k_B T}{h^2}\right)^{3/2} \sqrt{I_1 I_2 I_3} \tag{3.11}$$

The vibrational partition function can be written as a product involving the vibrational frequencies v_i. The number of vibrations is $3N-6$ for a non-linear molecule, with N being the number of atoms.

$$q_{vib} = \prod_{i=1}^{3N-6} \frac{e^{-hv_i/2k_BT}}{1-e^{-hv_i/k_BT}} \tag{3.12}$$

The partition function for the electronic degree of freedom is a sum of all quantum states. However, since the energy difference between the ground and excited states is typically large compared to k_BT, only the ground state becomes important. This means that the partition function can be approximated by only the ground state.

$$q_{elec} = \sum_{i=0}^{\infty} g_i e^{-\epsilon_i/k_BT} \approx g_0 e^{-\epsilon_0/k_BT} \tag{3.13}$$

Defining the ground state energy as the zero-point energy, the partition function becomes equal to the degeneracy g_i.
For surface-bound atoms, the contribution from the translation and rotation degree of freedom is typically assumed to be small since the movement is restricted. In this case, the entropy is calculated from the vibrational frequencies. However, for zeolites, this becomes challenging since the species may contain a significant amount of translation and rotational entropy.[77] The previous sections have shown how to add temperature and pressure effects for static structures that correspond to zero kelvin. At finite temperatures, the system becomes dynamic and the molecules move, which can be modeled using molecular dynamics.

3.5 Molecular Dynamics

In molecular dynamics (MD), the motion of the atoms is simulated at elevated temperatures and pressures. The nuclei are typically heavy enough to be approximated as classical particles. The motion can in this case be described by Newton's second law.

$$F = ma \tag{3.14}$$

F is the force, m is mass and a is acceleration. Newton's equations of motion for a set of atoms can be solved numerically using the Verlet algorithm.[78] Here r_i is the initial position and r_{i+1} is the new position.

$$r_{i+1} = (2r_i - r_{i-1}) + \frac{F_i}{m_i}\Delta t^2 \tag{3.15}$$

Δt is the timestep. If the force is evaluated using first-principle calculations, it is called ab initio molecular dynamics (AIMD).[79] The force can also be estimated using ML-FF from which simulation times in the range of nanoseconds can be achieved. The choice of the timestep Δt, depends on the application. A large timestep allows for long simulation times, as the forces have to be evaluated less frequently. However, a too large timestep can lead to inaccuracies in the simulation as rapid changes may not be captured. The choice of timestep typically depends on the lightest atom

included in the simulation, as they vibrate faster, a smaller timestep is, therefore, needed for systems containing hydrogen atoms. If the vibration of the hydrogen atoms is not of interest, they may be slowed down by increasing the mass or simply freezing the bond length, allowing a higher time step.[52]
To mimic experimental conditions in the MD simulations, different thermodynamic ensembles exist that are coupled to the surroundings in different ways. The simplest one is the microcanonical ensemble (NVE), where the system has a constant number of atoms, volume, and energy. Typically an experiment can exchange heat with the surroundings, and in this case, an NVT ensemble is a more suitable choice, where instead of the energy, the temperature is kept constant. A third option encountered in MD simulation is the NPT ensemble where the pressure is kept constant, hence the volume is allowed to change. In reality, the temperature is not fixed at all times but fluctuates around the target temperature, controlled by a thermostat. A popular thermostat is the Nosé-hoover thermostat,[80,81] which is used in this thesis. Here a heat bath is coupled to the physical system via the Lagrangian.

$$L = \sum_{i=1}^{N} \frac{m_i}{2} s^2 \left(\frac{dr_i}{dt}\right)^2 - U(r) + \frac{Q}{2}\left(\frac{s}{dt}\right)^2 - g k_B T \ln s \tag{3.16}$$

The first two terms correspond to the kinetic and potential energy of the system, respectively. The variable s introduces an extra degree of freedom into the system, Q is the effective mass of s and g is the number of degrees of freedom of the system ($g = 3N$, where N is the number of atoms).

The output of an MD simulation is a trajectory, which contains the evolution of the system. Several important properties can be extracted from this trajectory. Two common analytical properties are mean squared displacement (MSD) and radial distribution function (RDF).[82] The MSD analysis can be used to estimate the mobility of molecules. It measures the average displacement of a molecule from its reference position over the entire simulation as a function of time. MSD can be calculated as follows:

$$MSD(\tau) = \frac{1}{N}\sum_{i=1}^{N}\frac{1}{M}\sum_{j=1}^{M}\left|\mathbf{r}_i(\tau_j + \tau) - \mathbf{r}_i(\tau_j)\right|^2 \tag{3.17}$$

N is the number of molecules, M is the number of time intervals, r_i is the position of molecule i, and τ is the time interval. An example of an MSD plot calculated for the diffusion of a $[Cu(NH_3)_2]^+$ complex for different zeolite compositions is shown in Figure 3.1. The initial increase in Å^2 at low τ is due to the free motion of the complex. Based on the MSD plot, it can be concluded that for a higher Cu/Al ratio the $[Cu(NH_3)_2]^+$ complexes has a increased mobility.

RDF, measures the probability of finding a given atom at a specific distance from a reference atom. It can be used to find patterns in the interatomic distances, which may provide insight into the physical properties of the system. Figure 3.2 illustrates the process of constructing an RDF plot for the Cu-Cu distance. Figure 3.2(a) is a histogram for the frequency of finding another Cu ion within a certain radius interval, sampled over a 5 ns simulation. In general, the frequency increases

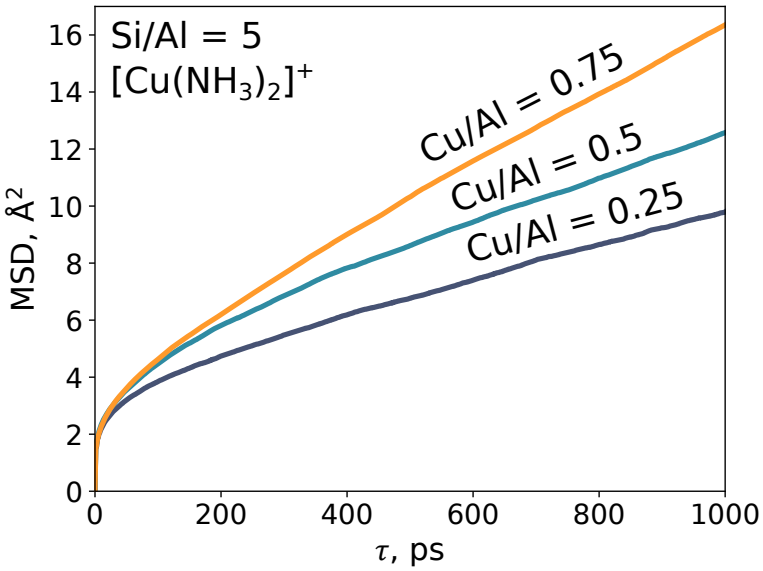

Figure 3.1: Mean squared displacement (MSD) analysis for $[Cu(NH_3)_2]^+$ at different zeolite compositions with Si/Al set to 5.

with distance because the sampled volume grows with radius. The sampled region corresponds to the volume of a spherical shell at that radius interval. The histogram is normalized as follows.

$$g(r) = \frac{H(r)}{(N_{total}/V_{cell})V_{shell}(r)} \tag{3.18}$$

Here, $g(r)$ is the RDF which is now normalized and $H(r)$ is the histogram. N_{total} is the total number of species studied, in this case Cu atoms, and V_{sphere} is the volume of the full sphere that is analyzed. This makes (N_{total}/V_{sphere}) the average number density of Cu atoms. $V_{shell}(r)$ is the volume that is sampled in the spherical shell at radius r. The denominator represents the expected number of atoms within the sampled spherical shell if they are randomly distributed. Therefore, at larger distances, when interactions between atoms are weak or absent, $g(r)$ converges towards 1.

In Figure 3.2(c), the bin size (Δr) of the histogram is reduced and plotted as a line. Finally, in Figure 3.2(d), the RDF of all Cu species are averaged. Here, two peaks are observed at approximately 5.2 and 7.9 Å. The first peak corresponds to two Cu complexes being in the same CHA cage, and the second peak corresponds to two Cu species in two adjacent CHA cages. The increase in intensity from the first to the second peak suggests that the two Cu ions repel each other when they are close. Lastly, the free energy landscape can be derived from MD simulations provided that the relevant transition happens frequently enough. This can be computed by constructing a histogram as a function of the reaction coordinate, x and computing the free energy, $F(x)$ as follows.[83]

$$F(x) = -k_B T \ln H(x) \tag{3.19}$$

k_B is the Boltzmann constant, T is the temperature and $H(x)$ is the histogram.

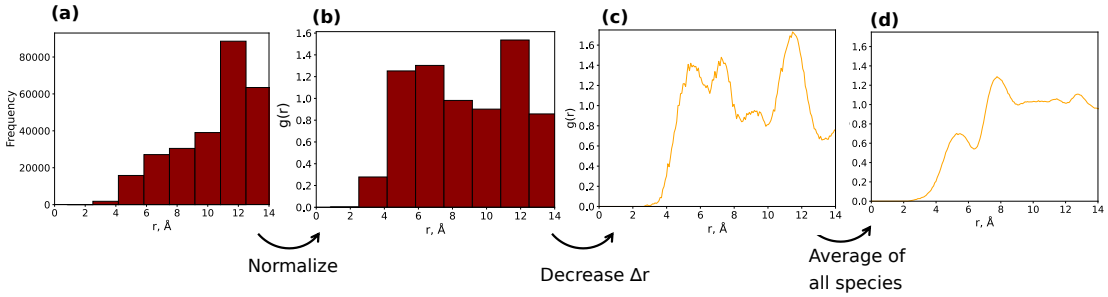

Figure 3.2: Procedure for how to construct a radial distribution function (RDF). (a): histogram for Cu-Cu distances. (b): Normalized RDF that is shown as a histogram. (c): RDF plotted as a line. (d): RDF that is an average over all Cu species in the simulation

In MD simulations, the atoms tend to stay around their minimum energy, and rare events may require a very long simulation time to be observed. The use of ML-FF to run MD simulations does improve this, but the problem still exists. To estimate the free energy barrier of rare events, a bias can be applied that forces the transition to happen more frequently, referred to as enhanced sampling techniques.

3.6 Enhanced Sampling Technique

Common for all enhanced sampling techniques is the need to define a collective variable (CV) that represents the reaction path for which the free energy is estimated. A simple CV could be a bond length, angle, torsion, or combinations of them. More advanced CV's include the Path Collective Variables,[84] where the CV is adapted to the lowest energy path connecting two structures. Furthermore, some approaches allows more than one CV to be explored. One example of a CV used in this thesis is shown in Figure 3.3. This CV describes the diffusion of a $[Cu(NH_3)_2]^+$ complex between two CHA cages connected by an eight-membered ring. A line is drawn through the eight-membered ring. The CV is then the position of the Cu along the line at which it intersects at 90°, shown by a red dot.

Two common methods used to sample the free energy barriers are slow growth[85] and metadynamics,[86] both of which are used in this thesis. In the slow-growth method, the CV is linearly changing from an initial value to a final value thereby, estimating the electronic energy along the reaction path. Using the blue moon approach, it is possible to estimate the free energy profiles.[87] Here, the free energy can be obtained by integrating the free energy gradients along the CV, ξ.

$$\Delta A_{1\to 2} = \int_{\xi(1)}^{\xi(2)} \left(\frac{\partial A}{\partial \xi}\right)_{\xi^*} d\xi \tag{3.20}$$

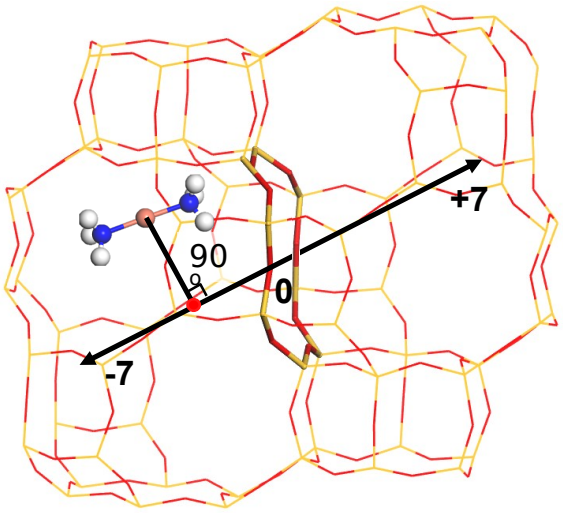

Figure 3.3: Illustration of a collective variable (CV) used for the diffusion of a $[Cu(NH_3)_2]^+$ complex between two CHA cages connected by an eight-membered ring used in **Paper V**. Atomic color codes: H(white), N(blue), O(red), Si(yellow) and Cu(Bronze).

3.6.1 Metadynamics

The idea behind metadynamics is that potential energy wells are filled with Gaussian functions, allowing for the sampling of rare events more frequently. In metadynamics, Gaussian functions are added during the simulation, where the bias V can be defined as:[88]

$$V(s,t) = \sum_{kr<t} W(k\tau) \exp\left(-\sum_{i=1}^{d} \frac{(s_i - s_i^{(0)}(k\tau))^2}{2\sigma_i}\right) \tag{3.21}$$

The bias $V(s,t)$, is added to the potential energy landscape, which can force the molecule through transitions that otherwise would not happen during the timescale of the simulation. W and σ are the width and height of the Gaussian function, s and s^0 are the values of the CV and the CV where the Gaussian function is added, respectively. A popular version of the method is well-tempered metadynamics[86], where the height of the Gaussian W decreases over time, resulting in a smoother convergence. In the long time limit, the bias potential should converge to the negative Helmholtz free energy F, with a constant C.

$$V(s, t \to \infty) = -F + C \tag{3.22}$$

The free energy can be estimated directly from the added Gaussian as shown in (3.22). In cases where one is interested in studying other CVs than what has been used in the simulations, it is possible to reweight the bias.[89] Figure 3.4(a) shows the free energy estimates at different times. As the simulation time increases the free energy profiles at different times should converge. The exploring of the CV during the simulation is illustrated in Figure 3.4(b). The system oscillates around the reaction path, slowly refining the free energy profiles. As the simulation is performed with well-tempered metadynamics, the height of the Gaussians as a function of simulation

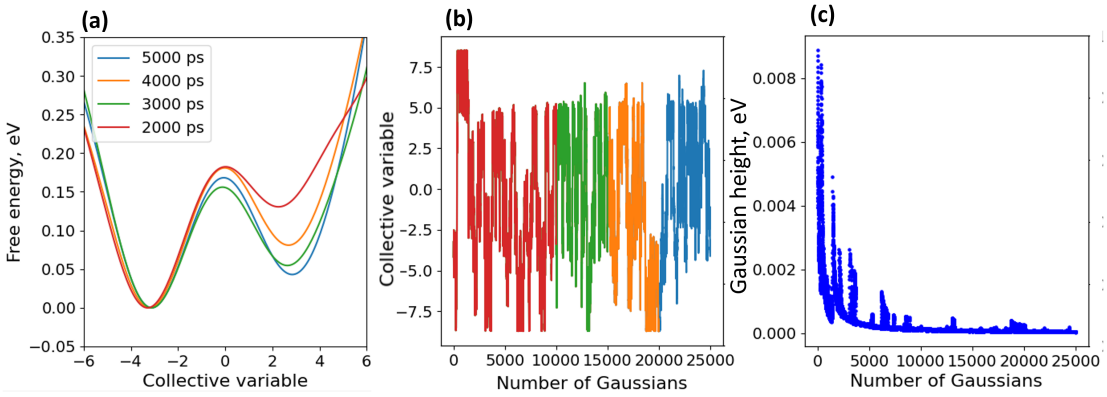

Figure 3.4: Well-tempered metadynamics simulations. (a): Estimated free energy profiles calculated at different simulation times. (b): Value of the CV for every Gaussian function deposited during the simulation. (c): Height of the Gaussian during the simulation.

time decreases, see Figure 3.4(c). The idea behind well-tempered metadynamics is that the first Gaussian functions are used to fill up the potential energy wells and a high Gaussian height makes the sampling faster. When the potential energy wells are filled, smaller Gaussian functions are used to refine the free energy profile which should lead to a smooth convergence in the long time limit.[86] To speed up the metadynamics simulation, it is possible to run several MD simulations simultaneously, referred to as the multiple walker method.[90] Each walker (MD simulation) deposits Gaussian functions that are shared with the other walkers, resulting in a single free energy landscape.

4

Kinetic Modelling

ML-FF enables simulations close to the microsecond time scale, however, typical catalytic turnover occur over much longer periods. Kinetic modelling can be used to study the evolution of chemical reactions over extended timescales, which makes it possible to compare with experiments. In this chapter, the mean field approximation is introduced, along with its extension to reactor models and how the rate constants can be evaluated.

4.1 Reaction Kinetics

Reaction kinetics is the study of the rates of chemical reactions and can provide a link between the mechanism and experimental observations. The rate, r can phenomenologically be expressed as follows.

$$r = k p_A^a p_B^b \tag{4.1}$$

k is the rate constant. p_A and p_B are the gas pressures of species A and B, respectively, with a and b being the reaction orders. The rate constant increases with temperature, as highlighted, for example, in the Arrhenius equation 1.1.
A simple reaction can be A and B adsorbing as AB forming the product P.

$$A + B \rightarrow AB \rightarrow P \tag{4.2}$$

Such reactions can be divided into elementary reactions and global reactions. Elementary reactions represent individual events, such as adsorption, desorption, and surface reaction. The reaction order follows the stoichiometry of the step, and the rate constants can be derived from first-principle calculations. First-principle based microkinetic models make use of elementary reaction steps, as they explicitly account for each reaction step and its associated kinetics. Global reactions lump multiple elementary steps, simplifying them into a single overall reaction. Since they consist of multiple reactions, the reaction order is not necessarily based on the stoichiometry of the step and can take non-integer values. Global reactions are typically used in phenomenological models, where the kinetic parameters are derived using experiments. The advantages of first-principle based microkinetic models are that they provide insight into the atomistic mechanism, which can be used to rationalize different behaviors. However, they can also be computationally expensive to construct due to expensive first-principle calculations needed to derive the rate constant. In contrast, phenomenological models can be simpler to apply to complex reactions, but they lack the atomistic insight provided by first-principle based

microkinetic models. They are particularly advantageous when overall performance is more important than the details of individual elementary steps. For both types, the mean-field approximation is one of the most popular approaches for kinetic modelling.

4.1.1 Mean-field Model

In the mean-field approximation, it is assumed that all species are distributed randomly on the surface. This is strictly valid only in the absence of interactions between the adsorbed species.[91] In reality, adsorbate-adsorbate interactions are often present. The approximation especially fails for systems with strong attractive forces, since the adsorbed species tend to cluster and form islands on the surface rather than being randomly distributed. The advantage of the mean-field model is its simplicity, which makes it relatively fast and straightforward to interpret and analyse.

To simulate the system, a set of ordinary differential equations (ODE) is solved.

$$\frac{d\theta_i}{dt} = \sum_j v_{ij} r_j \tag{4.3}$$

θ_i is the coverage of species i, v_{ij} is the stoichiometric coefficient for reaction j, and species i. r_j is the rate of reaction j and is given by the rate constant k and coverage θ.

$$r_j = k_j^f \prod_f \theta_f - k_j^r \prod_b \theta_b \tag{4.4}$$

If a temperature ramp is applied, such as in the case of temperature-programmed reduction analysis, a time-dependent temperature, assuming a linear heat rate, is used for the microkinetic modelling.

$$T = T_0 + \beta t \tag{4.5}$$

T_0 is the starting temperature, β is the heating rate and t is the time.

4.2 Reactor Model

The mean field approximation allows for simulation of the intrinsic reaction rates, however, for simulating catalytic reactors, additional considerations are required, such as transport, flow and heat and mass transfer effects. One example of a catalytic reactor is a monolith, where the catalyst is supported on a structured substrate. A monolith consists of many parallel channels, which are coated with catalytic materials. The large number of channels ensures a high surface area, combined with a low pressure drop, making them suitable for use in automotive exhaust treatment systems.

To model a reactor, three common assumptions are typically used to describe three simple reactor types: the batch reactor, the plug flow reactor (PFR), and the continuous stirred-tank reactor (CSTR).[92] A batch reactor is a closed, non-continuous

chemical reactor with no flow of reactants or products. A plug flow reactor is a continuous reactor in which the reactant moves as a plug through the reactor, with no back mixing. As a result, the reactor will have a temperature and concentration gradient. In a CSTR, the concentration is constant throughout the reactor, hence the outlet has the same composition as inside the reactor. For more complicated systems, the reactor can be discretized along the reactor length, dividing it into small segments, represented as a set of coupled ordinary differential equations (ODEs). This approach is used in **Paper IV** and **VI**

4.3 Evaluation of Rate Constants

Two approaches are used to evaluate the rate constants in this thesis, namely fitting to experimental data and evaluation by first-principles calculations.

In a phenomenological kinetic model, the rate constant is typically described by the Arrhenius equation (1.1), in which the prefactor and barrier are fitted to experiments. In addition, the reaction order may also be fitted if necessary. This can be done by defining an objective (loss) function that describes the difference between the simulated and experimental results. The result could, for example, be the outlet concentration or the amount adsorbed of a specific gas. The fitting is then a minimization problem, where the parameters are tuned such that the lowest objective function is achieved. This is typically done using global reaction steps, since it can be difficult to resolve the kinetics in a detailed mechanistic model. For instance, if an elementary reaction has little to no degree of rate control, fitting its rate constant based on experiment can be challenging.

Typically, the experiments are designed to extract specific rate constants and/or reaction orders. Take, for example, the kinetic model shown in Figure 4.1 from **Paper VI**. This model is developed to describe NH_3-SCR, which is a redox reaction. It includes reduced Cu^{I} and oxidized Cu^{II}, and NH_3 can adsorb onto Cu^{II} to form $Cu^{II}-NH_3$. The parameters for R3, which describe the oxidation of Cu^{I} to Cu^{II}, are fitted using steady state experiments at different O_2 concentrations. R4 is the reduction of Cu^{II} to Cu^{I} and is fitted based on steady state experiments at different NH_3 concentrations. Alternatively, oxidation and reduction half-cycle experiments could be used to fit the kinetics of these steps more directly. Finally, R5 is primarily fitted to transient response experiments designed to investigate the adsorption of NH_3 on Cu^{II}.

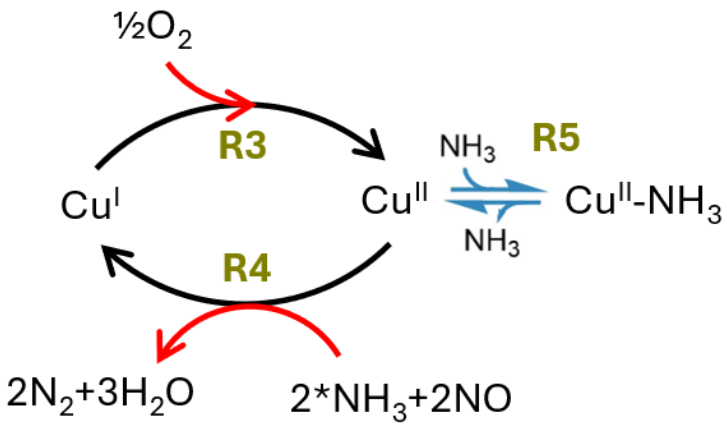

Figure 4.1: Illustration of a reaction mechanism for a phenomenological kinetic model used in **Paper VI**.

In first-principles based microkinetic models, the elementary steps and their energetics are calculated using methods such as DFT, which are then used to compute the rate constant using transition state theory (TST)[93].

$$k = \frac{k_B T}{h} e^{-\Delta G^{\ddagger}/k_B T} \tag{4.6}$$

$\Delta G^{\ddagger}$ is the free Gibbs energy difference between the transition state and initial state. The change in Gibbs free energy can be calculated from the enthalpy and entropy.

$$\Delta G = \Delta H - T\Delta S \tag{4.7}$$

The enthalpy can be approximated as the zero point corrected electronic energy E by neglecting the pV-dependence. The entropy can be calculated using partition functions as introduced in Section 3.4. Note that the reaction coordinate should be excluded from the partition function of the transition state. Combining equation 4.6 and 4.7, the rate constant becomes:

$$k = \frac{k_B T}{h} e^{-\Delta H^{\ddagger}/k_B T} e^{\Delta S^{\ddagger}/k_B} \approx \frac{k_B T}{h} e^{-\Delta E^{\ddagger}/k_B T} e^{\Delta S^{\ddagger}/k_B} \tag{4.8}$$

For adsorption reactions, the rate constant can be calculated using collision theory.

$$k = \frac{pA}{\sqrt{2\pi m k_B T}} e^{-E^{\ddagger}/k_B T} \tag{4.9}$$

A is the area of the active site, p is the partial pressure, and m is the mass. To ensure thermodynamic consistency, the reverse rate constant is calculated from the equilibrium constant

$$K = \frac{k_f}{k_r} = e^{-\Delta G/k_B T} \tag{4.10}$$

k_f and k_r are the forward and reverse rate constants, respectively, and ΔG is the free Gibbs energy change between the final and initial states.

5

Characterization of Cu Species

Cu-ions can in Cu-CHA have different oxidation states (Cu^{I} and Cu^{II}) and be solvated by different ligands (H_2O, NH_3). Thus, the state of the Cu-ions depends sensitively on the temperature and feed-gas.[43] Different methods exist for quantifying Cu species in Cu-CHA, including infrared (IR), Ultraviolet–visible (UV–vis) and X-ray absorption (XAS) spectroscopy.[94,95] Another method is temperature programmed reduction with hydrogen (H_2-TPR), which is studied and used in **Paper I**. The H_2-TPR profiles are, however, often complex with overlapping peaks, making the interpretation difficult. By comparing experimental and computed TPR profiles, we show that it is possible to gain new insights into the dominant Cu species in Cu-CHA.

The chemical state of the Cu ions has implications for the catalytic performance. For example, at low temperature, the NH_3-SCR reaction proceeds over NH_3 solvated Cu ions, whereas at high temperature it proceeds over framework bound Cu ions.[34] The solvation also affects the mobility of Cu ions[96]. NH_3 solvated Cu^{I} ions, in particular, have a high mobility and can diffuse between cages. Because O_2 adsorption in the low-temperature mechanism requires two $[Cu(NH_3)_2]^+$ complexes in the same cage, it is critical to understand diffusion and pairing of the complexes, which is studied in **Paper V**.

5.1 State of Cu during Operating Conditions

H_2-TPR has mainly been used to characterize two different Cu sites, ZCuOH and Z_2Cu. Here, Z represents a one-Al environment and Z_2 a two-Al environment. H_2 consumption at 210 °C is usually attributed to ZCuOH and consumption at 320 or 480 °C is mainly attributed to Z_2Cu. However, the interpretation is not fully settled[39,94,97–101], and the H_2-TPR profiles may have different shapes and peaks depending on the pre-treatment and zeolite composition, making the interpretation complex.

Numerous Cu species have been identified, but only a few have been discussed in relation to H_2-TPR profiles. This includes NH_3 solvated Cu species such as $[Cu(NH_3)_2]^+$ and $[Cu_2O_2(NH_3)_4]^{2+}$, that are important intermediates in the NH_3-SCR reaction.[31,33] Different framework-bound Cu species may also exist, such as $Z_2CuOOCu$, $Z_2CuHOOHCu$, and Z_2CuOCu, which have been proposed to be important for the methane-to-methanol reaction.[102–104] While ZCuOH and Z_2Cu previously have been studied extensively in the context of H_2-TPR, there is a limited understanding of which temperatures the alternative Cu sites consume H_2.

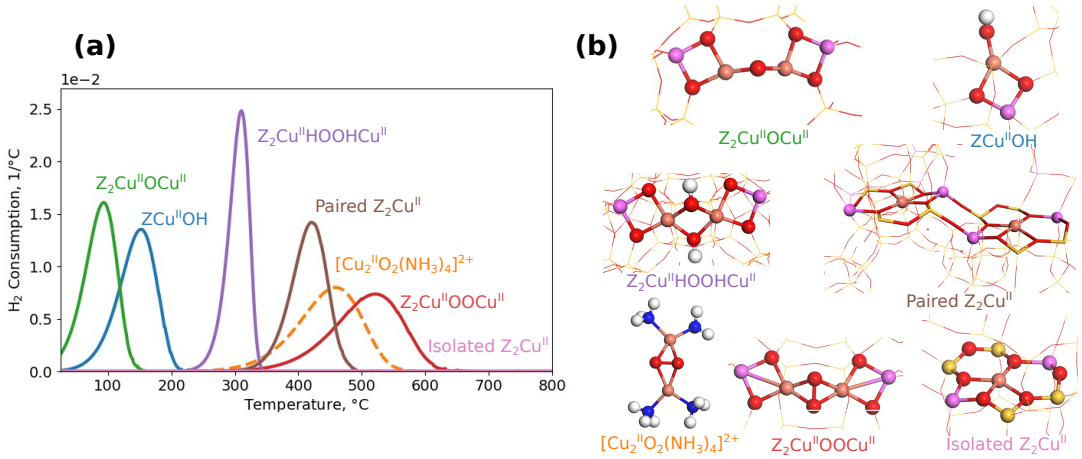

Figure 5.1: (a): Simulated H_2-TPR profiles. (b): Cu species considered in the simulation. Atomic color codes: H (white), N (blue), O (red), Al (purple), Si (yellow), and Cu (bronze).

In **Paper I**, a new method is developed to simulate H_2-TPR profiles that can aid the interpretation of experiments. The approach is based on a first-principles microkinetic model with rate constants calculated using DFT data. The simulated H_2-TPR profiles are shown in Figure 5.1(a) with the Cu sites shown in Figure 5.1(b). Cu in oxidation state +1 is also considered, however, no energetical favored pathway is found for the adsorption of H_2 on Cu^I species, although they are reported to be reduced at high temperatures in the literature.[97] This discrepancy may be explained by the fact that Cu^I is commonly assigned to TPR signatures above 800 °C, where the destruction of the framework may occur, which is not taken into account in our calculations.[99]. Our simulated H_2-TPR profiles predict that ZCuOH reduces at 150 °C and Z_2Cu at 420 °C, which is consistent with literature.[39,94,97–101] However, it is also observed that the measured H_2-TPR profiles potentially could be assigned to other Cu sites such as Z_2CuOCu, $Z_2CuHOOHCu$ and $Z_2CuOOCu$, as they adsorb H_2 in similar temperature ranges. One notable finding is that only two proximate Z_2Cu sites can be reduced with H_2, thus, a single isolated Z_2Cu site should not be reduced. This highlights the important role of the Al distribution in determining reduction temperatures.

5.1.1 Influence of Al Distribution

The DFT calculations are performed at a specific Al distribution, however, many combinations exist, which may influence the reaction landscape. To investigate this, H_2-TPR simulations are carried out for two sites, Z_2Cu and $Z_2CuOOCu$, using different Al configurations. The Al distributions are shown in Figure 5.2(a) and the simulated H_2-TPR profile in Figure 5.2(b). The simulated peaks are shifted 10 and 90 °C for Z_2Cu and $Z_2CuOOCu$, respectively. In reality, many combinations of Al placements are possible, and the experimentally observed reduction temperatures, represent an average over Cu sites with different local Al environments.

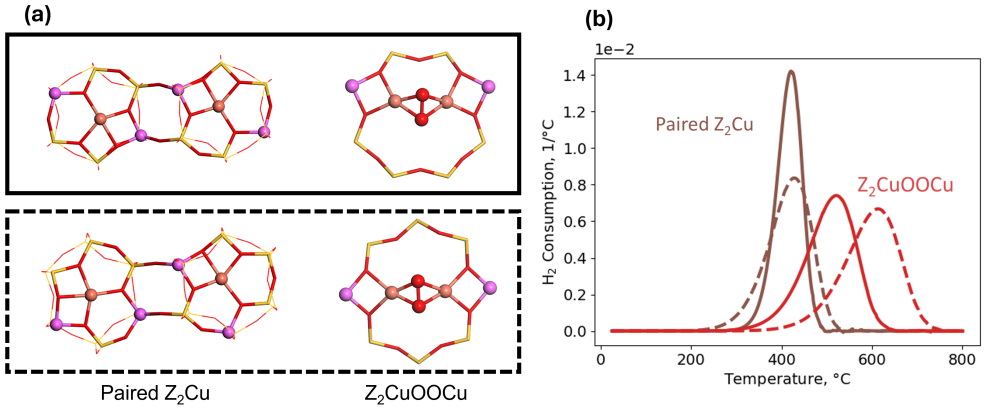

Figure 5.2: (a): Paired Z_2Cu and $Z_2CuOOCu$, shown with two different Al distributions. (b): Simulated H_2-TPR profiles for the species in (a), indicated with a dashed or solid line. Atomic color codes: O (red), Al (purple), Si (yellow), and Cu (bronze).

To further validate our findings, H_2-TPR experiments are performed on samples that are pretreated to contain well-defined Cu species. The experiments match the trends in our simulated profiles and further support our approach. This study shows that only considering ZCuOH and Z_2Cu when deconvoluting H_2-TPR profiles may not capture the full experimental situation.

5.2 Mobility of $[Cu(NH_3)_2]^+$ Complexes

The mobility of $[Cu(NH_3)_2]^+$ complexes is important for the low-temperature NH_3-SCR as two $[Cu(NH_3)_2]^+$ complexes in the same cage are required for the adsorption and activation of O_2. The mobility of Cu complexes is not well understood, and can be challenging to investigate using experimental procedures. However, impedance spectroscopy has been used to investigate diffusion by tracking the dielectric relaxation process[105] associated with the diffusion of $[Cu(NH_3)_n]^+$. Electron paramagnetic resonance (EPR) spectroscopy has also been used to study the (super)hyperfine features, which relate to the dynamics of Cu ions.[106] The conclusions from the two experimental studies are that a higher Cu loading leads to increasing Cu mobility, whereas at lower Cu loadings, the diffusion of Cu species becomes rate controlling for the NH_3-SCR activity. Although the experiments provide important information, an atomistic understanding of the mobility and dynamics of Cu^I species is currently accessible only through computational studies. There have been several studies using ab initio molecular dynamics (AIMD) to estimate free energy barriers,[31,107] however, such studies are limited to small system sizes and short simulation times. The use of machine learning force field (ML-FF) makes it possible to study properties inaccessible to conventional AIMD simulations.[108] In **Paper IV**, an ML-FF augmented with long-range electrostatic is constructed to investigate the diffusion of $[Cu(NH_3)_2]^+$ in Cu-CHA.

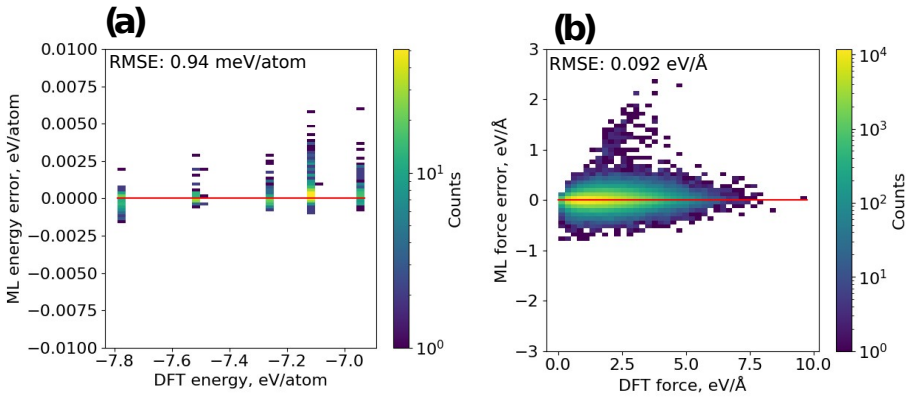

Figure 5.3: Validation of the machine learning force field (ML-FF). (a): Correlation between ML-FF and DFT energies (b): Correlation between predicted and DFT forces.

The training data for the ML-FF are gathered by constructing a variety of structures with different numbers of $[Cu(NH_3)_2]^+$, NH_4^+ and Al atoms, different Al distributions, and different unit cell sizes. The final ML-FF is based on approximately 52000 single-point DFT calculations covering a wide chemical space. To assess the accuracy of the ML-FF, a new set of data is created from new structures that are not used in the training of the ML-FF. This ensures that the ML-FF can extrapolate to new Al distributions and new combinations of $[Cu(NH_3)_2]^+$ and NH_4^+. The predicted energies and forces are compared to DFT calculations and the comparison is shown in Figure 5.3. The calculated root mean squared error is 0.94 meV/atom for the energies and 0.092 eV/Å for the forces, indicating that the ML-FF is robust.

5.2.1 Collective Effects

The cations ($[Cu(NH_3)_2]^+$ and NH_4^+) are counterbalanced by anionic Al ions. This means that they are tethered to their Al ion and long-distance movement requires an ion-exchange process to maintain local charge neutrality. Because of this, the mobility of the ions can be expected to influence each other. To investigate such effects, metadynamics simulations are performed using two collective variables (CV), being the movement of a $[Cu(NH_3)_2]^+$ complex and a NH_4^+ ion. The resulting three-dimensional landscape is shown in Figure 5.4(a) with selected minimum free energy paths illustrated in Figure 5.4(b). The stable and metastable structures are indicated with a letter corresponding to a specific structure in 5.4(c). A negative CV for $[Cu(NH_3)_2]^+$ complex corresponds to two isolated Cu ions, whereas a positive CV corresponds to paired Cu complexes in the same cage. The three different minimum free energy paths represent the pairing of two Cu complexes with different locations of the NH_4^+ ion.
If the NH_4^+ has a CV ~ 8, the free energy barrier for pairing (A $\rightarrow$ B) is 0.48 eV, with the isolated and paired Cu ions having similar stability. If the NH_4^+ ion moves to a CV of ~ 4, the free energy barrier (C $\rightarrow$ D) is 0.42 eV, with the paired Cu

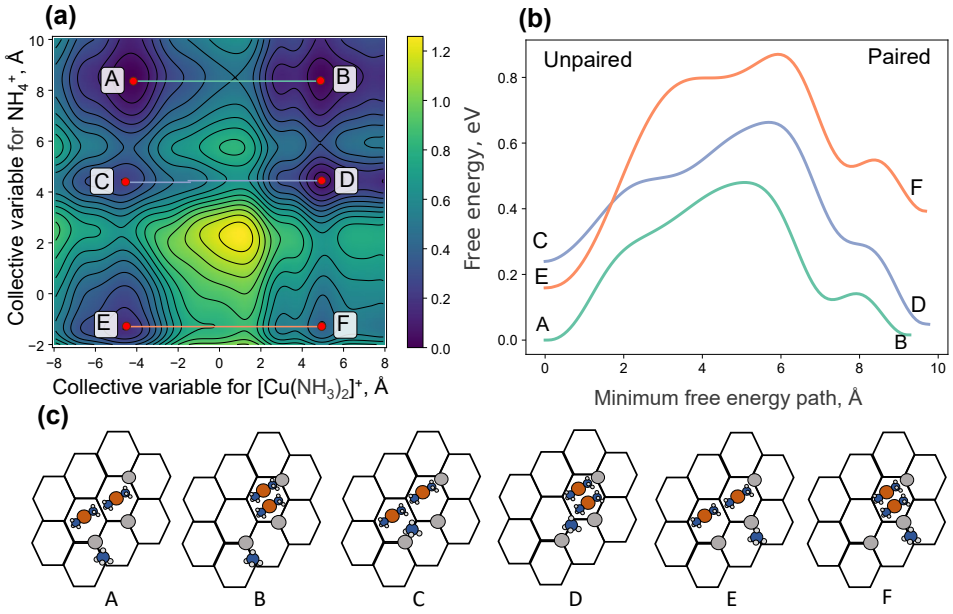

Figure 5.4: Metadynmics simulation with two collective variables. Stable and metastable structures are labeled with letters (A-F) (a): free energy landscape. (b): Selected minimum free energy paths. (c): Location of $[Cu(NH_3)_2]^+$ and NH_4^+ for the different structures.

complex stabilized by -0.19 eV. For the last minima of NH_4^+ corresponding to a CV of ~ -1, the free energy barrier (E $\rightarrow$ F) is 0.71 eV, and the isolated Cu species is preferred by 0.24 eV. These results highlight the importance of collective effects between the charged ions, which can dramatically alter the free energy landscape, even when two cations are not in the same cage. Under practical conditions, the Cu-CHA system contains many cations, and their correlated movements make the system coupled and challenging to investigate.

5.2.2 Influence of Zeolite Composition

To investigate the influence of zeolite composition, unbiased MD simulations are performed at different Si/Al and Cu/Al ratios. From the trajectories, the fraction of paired $[Cu(NH_3)_2]^+$ complexes is computed and shown in Figure 5.5 for different zeolite compositions. As paired $[Cu(NH_3)_2]^+$ complexes are required for O_2 adsorption, a higher fraction of paired complexes is expected to correlate with higher catalytic activity.

For a Si/Al ratio of 5, shown in Figure 5.5(a), a Cu/Al ratio of 0.75 exhibits the highest fraction of paired $[Cu(NH_3)_2]^+$ complexes. The dashed line shows the fraction of paired $[Cu(NH_3)_2]^+$ complexes if they were randomly distributed. For Cu/Al ratios of 0.75 and 0.5, the simulated fraction of paired complexes is below the dashed line, indicating that the paired state is more unstable than a random distribution, likely due to the repulsion between the Cu ions. Interestingly, this is not the case for a Cu/Al ratio of 0.25 where the simulated fraction exceeds the dashed line after approximately 1-2 ns. At this low Cu/Al ratio, there are more Al and NH_4^+ per

Cu, which may help to stabilize the paired complexes.
For a Si/Al of 13 [Figure 5.5(b)], the same trend is observed for the different Cu/Al ratios, where higher values result in a larger fraction of paired Cu complexes. However, compared to the case with Si/Al 5, the simulated fraction of paired Cu complexes is significantly lower than the random distribution. This suggests that the higher amount of Al and $NH_4{}^+$ for a Si/Al ratio of 5 promotes pairing. To isolate the influence of Al and $NH_4{}^+$, MD simulations are performed with a fixed number of Cu ions while only changing the Si/Al ratio. This is shown in Figure 5.5(c), and here it is clear that additional Al and $NH_4{}^+$ increase the fraction of paired Cu ions.

Finally, Figure 5.5(d) shows a histogram for the lifetime of the paired $[Cu(NH_3)_2]^+$ complexes. The lifetime spans from less than 0.1 ns up to almost 3.5 ns. This suggests that some $[Cu(NH_3)_2]^+$ pairs are in a more stable configuration than others. This emphasizes the importance of the local environment, which may be influenced by favorable Al distributions or by collective effects between the cations. The lifetime of the pairs can be compared to the timescale of O_2 adsorption, which is $10^8 s^{-1}$ at standard conditions based on collision theory. This corresponds to an average time of 10 ns between each O_2 adsorption event, thus, $[Cu(NH_3)_2]^+$ complexes can be assumed to be paired and separated multiple times before adsorbing O_2. This suggests that the NH_3-SCR activity is not limited by the rate of complex diffusion but rather the stability between the separated and paired states.

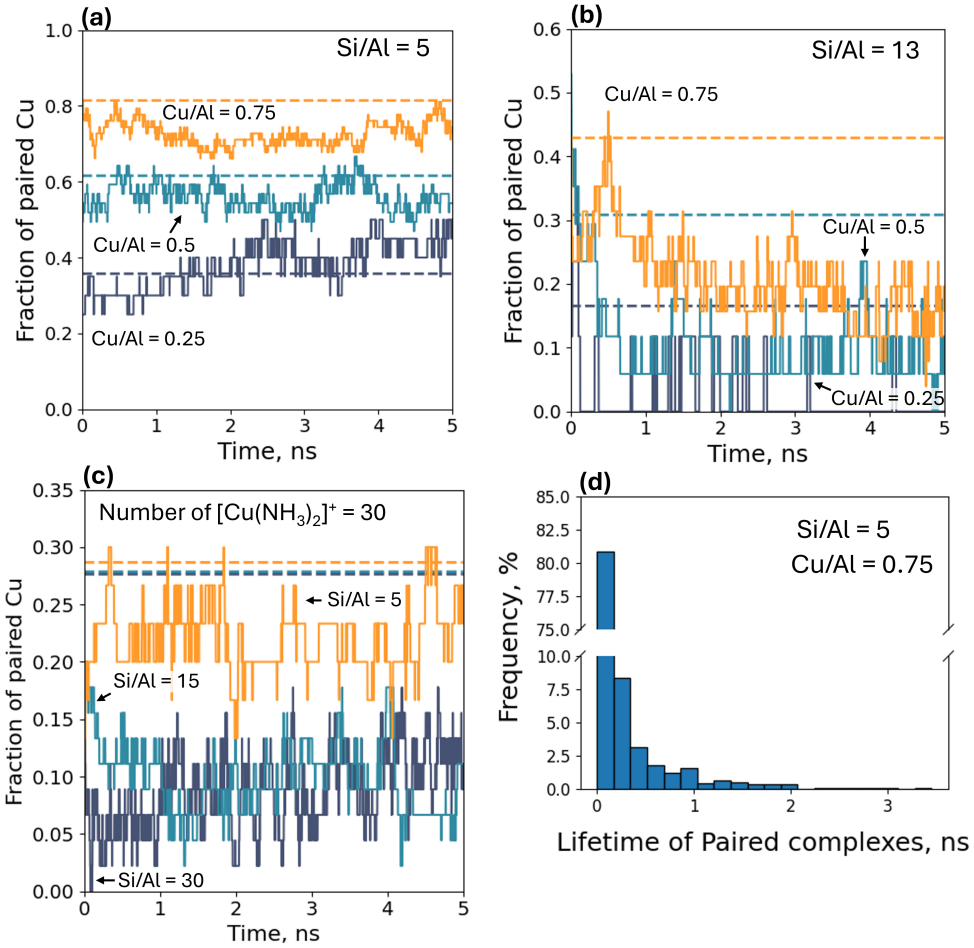

Figure 5.5: Fraction of paired Cu complexes as a function of time for a Si/Al of (a) 5 and (b) 13, and (c) with a fixed number of Cu ions (30). (d): Histogram for the lifetime of Cu pairs for a composition of Si/Al=5 and Cu/Al=0.75.

6

Sulfur Poisoning during NH_3-SCR

As discussed in the Introduction, the catalyst is exposed to small amounts of SO_2 and SO_3, which poison the catalyst and reduce its activity. To develop strategies for mitigating sulfur poisoning, it is essential to understand the underlying mechanisms. The sulfur poisoning is studied for low temperatures in **Paper II** and high temperatures in **Paper III**, using DFT calculations. The insights from the DFT calculations are used to develop a kinetic model describing sulfur poisoning in **Paper IV**.

For Cu-CHA samples with low Cu loading, the NH_3-SCR activity as a function of temperature typically shows a minimum referred to as the seagull shape.[109] This is attributed to two different reaction mechanisms, at low and high temperatures. The reaction mechanisms reflect different states of Cu present in the two different temperature regimes. The reaction proceeds over $[Cu(NH_3)_2]^+$ species at low temperatures, whereas framework-bound Cu species are active sites at high temperatures.[34] Different Cu species are expected to have different reactivity towards sulfur.

The current understanding of the interaction of SO_2 and SO_3 species with Cu-CHA on the atomic level is limited. Previous studies have mostly been focused on ZCuOH and Z_2Cu,[39], which are species that are present at high temperatures. As SO_2 does not adsorb in Cu-free chabazite (H-CHA)[39], the speciation of the Cu ions is likely to influence the sulfur deactivation. SO_2 temperature-programmed desorption (SO_2-TPD) is a common technique to quantify the sulfur-derived species formed upon SO_x exposure. The desorption of SO_2 at 420 °C is commonly assigned to the decomposition of $SO_4(NH_4)_2$ or $HSO_4(NH_4)$, and the two high-temperature peaks at 540 and 720 °C are assigned to sulfur bonded to Cu and Al.[110,111] Since SO_2 is released at 420 °C, the catalyst is periodically heated to approximately 500 °C to partially remove the sulfur species, thereby regaining some of the lost activity. The deactivation that can be recovered through the regeneration procedure is referred to as reversible deactivation, whereas the deactivation that remains after regeneration is referred to as irreversible deactivation.[38]

6.1 First-principle Mechanisms

6.1.1 Low-Temperature Deactivtion

Paper II investigates the reaction of SO_2 with Cu complexes present during low-temperature NH_3-SCR, such as $[Cu(NH_3)_2]^+$ and $[Cu_2O_2(NH_3)_4]^{2+}$. SO_2 does not to react with $[Cu(NH_3)_2]^+$ but with $[Cu_2O_2(NH_3)_4]^{2+}$ from which a detailed reac-

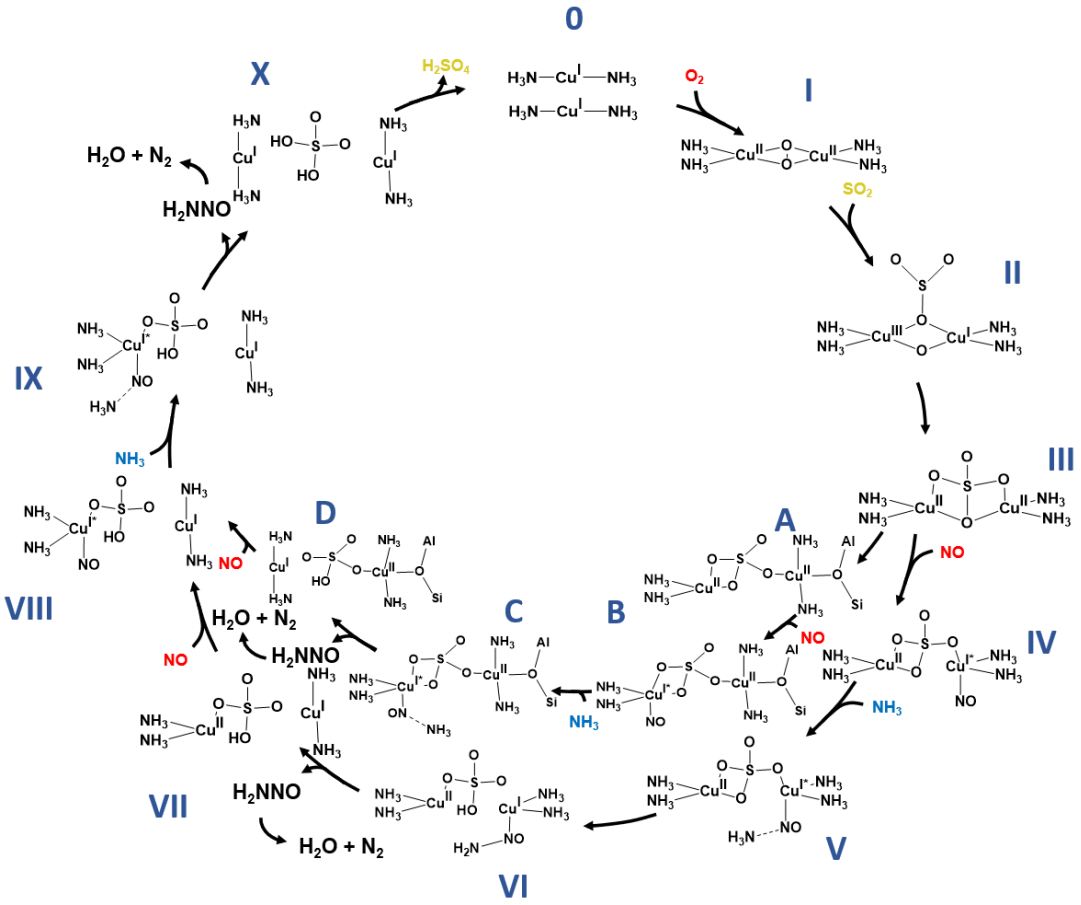

Figure 6.1: Proposed reaction cycle for the reaction of SO_2 with $[Cu_2(NH_3)_4O_2]^{2+}$ during low-temperature NH_3-SCR conditions. Al-O-Si represents a Brønsted site and is only shown if the complex is bonded to the framework.

tion mechanism is investigated and illustrated in Figure 6.1. The $[Cu_2O_2(NH_3)_4]^{2+}$ complex adsorbs SO_2 from structure I to II, leading to a stable Cu sulfate structure $[Cu_2(NH_3)_4SO_4]^{2+}$ (Structure III). NO and NH_3 can couple over the complex, forming H_2NNO that can decompose over a Brønsted site into N_2 and H_2O. In addition to N_2 and H_2O, H_2SO_4 is formed. The reaction can proceed via two routes, depending on whether it involves structures that are mobile (roman numbers) or bound to the framework (letters). As H_2SO_4 is a bulky molecule, it can not diffuse between chabazite cages due to a high diffusion barrier of 1.45 eV through the eight-membered ring and may accumulate, leading to a loss in activity. As NH_3 is present, H_2SO_4 can exchange protons forming $SO_4(NH_4)_2$ and $HSO_4(NH_4)$. Ab into thermodynamic analysis suggests that $HSO_4(NH_4)$ is the stable species at typical reaction conditions.

To investigate how the accumulation of $HSO_4(NH_4)$ affects the NH_3-SCR activity, constrained AIMD simulation is performed and the results are shown in Figure 6.2. The AIMD simulations are done to investigate the stability of paired $[Cu(NH_3)]^+$ complexes, which is necessary for the adsorption of O_2. If two ammonium bisulfate are present (red line), the stability of paired $[Cu(NH_3)_2]^+$ complexes is decreased,

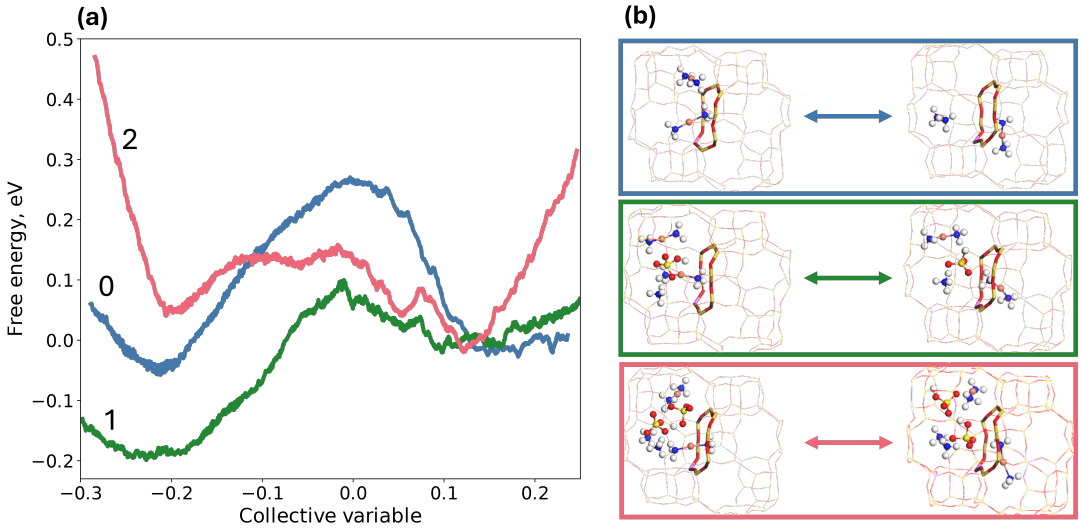

Figure 6.2: (a): Free energy profile for the diffusion of a $[Cu(NH_3)_2]^+$ complex through an eight-membered ring in the presence of a second $[Cu(NH_3)_2]^+$ complex and different numbers of ammonium bisulfates. (b): Snapshot of the initial and final state from the simulation. Atomic color codes: H (white), N (blue), O (red), Al (purple sticks), Si (dark yellow sticks), S (yellow), and Cu (bronze).

thus, deactivating the catalyst. This finding implies that the sulfur deactivation at low temperatures is of physical origin.

6.1.2 High-Temperature Deactivation

At higher temperatures, the $[Cu(NH_3)_2]^+$ complexes decompose and Cu binds to the framework. In **Paper III**, the sulfur poisoning was carried out at 400 °C, thus, only framework-bound Cu species are expected to be present. To investigate sulfur poisoning at this temperature, the interaction with both SO_2 and SO_3 is investigated for ZCuOH, Z_2Cu, and $Z_2CuOOCu$. Framework bound Cu^I is not found to adsorb or react with SO_x species similar to the case of $[Cu(NH_3)_2]^+$. Thus, Cu ions in oxidation state +1, are not active towards SO_2 or SO_3. Both low and high-temperature sulfur poisoning is illustrated in Figure 6.3. At low-temperature, there are the two complexes $[Cu(NH_3)_2]^+$ and $[Cu_2O_2(NH_3)_4]^{2+}$ discussed in the previous section. $[Cu(NH_3)_2]^+$ can not react with SO_2, whereas $[Cu_2O_2(NH_3)_4]^{2+}$ can couple with NH_3 and NO forming $HSO_4(NH_4)$ and $[Cu_2O_2(NH_3)_4]^{2+}$ is reduced back to two $[Cu(NH_3)_2]^+$ complexes. The main result from the high temperature reactions, is that SO_2 forms Cu sulfite species, whereas SO_3 forms Cu sulfate species. Formation of sulfates is more exothermic than the formation of sulfites. Experimentally it is also observed that SO_3 causes more severe catalyst deactivation than SO_2.[38] The reactivity of SO_x towards the framework bound species is in the order $Z_2CuOOCu$ > ZCuOH > Z_2Cu with $Z_2CuOOCu$ being most reactive. The formation of Cu sulfate blocks the Cu-sites by chemisorption, thus, high temperature deactivation is of chemical nature.

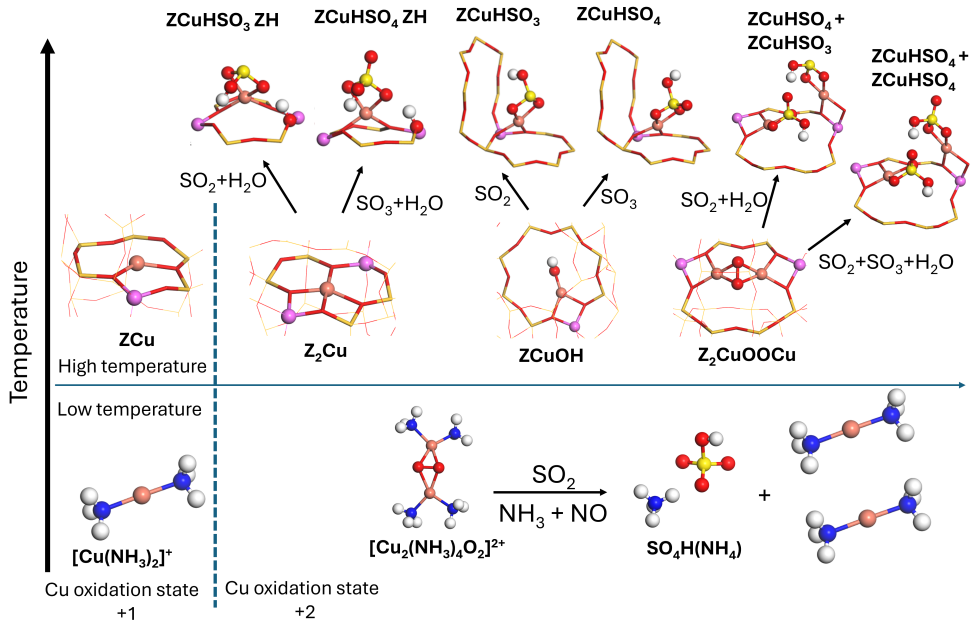

Figure 6.3: Overview of the Cu ions present at high and low temperatures for Cu oxidation state +1 and +2, together with the sulfur derived structure formed after SO_x exposure. Atomic color codes: H (white), N (blue), O (red), Al (purple), Si (dark yellow sticks), S (yellow), and Cu (bronze).

$HSO_4(NH_4)$ is commonly assigned to the SO_2 release in TPD at 420 °C, hence, this deactivation may be recovered by heating the catalyst. However, it has been suggested that a part of the ammonium sulfate may transform to strongly bound Cu or Al sulfates.[112] The Cu sulfate formed from the framework bound Cu species is expected to decompose at higher temperatures.

6.2 Modelling of Sulfur Deactivation

In paper **Paper IV**, we develop a kinetic model that is parameterized using reactor flow experiments for sulfur poisoning. The mechanism is inspired by some of the findings discussed in the previous sections, and is illustrated in Figure 6.4. The model is divided into two parts, reversible and irreversible deactivation, which correspond to the sites S_1 and S_2, respectively. S_1 can react with SO_2, NH_3, H_2O and O_2 to form ammonium bisulfate $S_1-HSO_4NH_4$. $S_1-HSO_4NH_4$ represent the accumulation of HSO_4NH_4 inside the cage as proposed in **Paper II**, hence S_1 represent the physical space inside in the CHA cage. $S_1-HSO_4NH_4$ can either decompose as SO_2, or transform into S_2-HSO_4. S_2-HSO_4 may be attributed to more strongly sulfur-bound complexes such as Cu sulfates, with examples shown in Figure 6.3. Another interpretation of the site could be related to Al sulfates[40]. S_2-HSO_4 can also decompose as SO_2, however, this requires significantly higher temperatures compared to the decomposition of $S_1-HSO_4NH_4$. As a result, S_2-HSO_4 is more likely to remain after thermal regeneration. The two sites $S_1-HSO_4NH_4$ and S_2-HSO_4

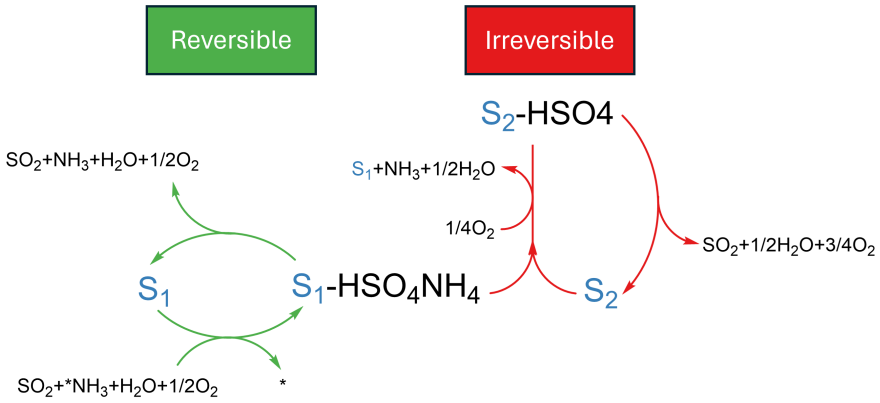

Figure 6.4: Kinetic model for describing sulfur deactivation.

deactivate the Cu-CHA catalyst through deactivation functions that are multiplied with the NH_3-SCR rates.
Figure 6.5(a), shows the deactivation as a function of time at three different temperatures during exposure of 30 ppm SO_2 in NH_3-SCR conditions. A clear temperature dependence is observed, with 200 °C being the most deactivated and the weakest 400 °C. The sulfur uptake follows the same trend, with significantly more SO_2 consumed at 200 °C.
The lower conversion at 400 °C can partly be attributed to the simultaneous decomposition of HSO_4NH_4, which occurs at similar temperatures.[110,111] However, this does not explain the lower deactivation at 300 °C. Our first-principle calculations in **Paper II** showed that the $[Cu_2O_2(NH_4)]_2^+$ reaction with SO_2 is exothermic. Furthermore X-ray absorption spectroscopy have shown that SO_2 is more reactive towards NH_3 solvated species like $[Cu_2O_2(NH_4)]_2^+$ compared to framework-bound Cu species.[95] This suggests that a higher sulfur adsorption at low temperature is related to the presence of more reactive NH_3 solvated Cu species.

To simulate more realistic conditions, cycles of sulfation and thermal regeneration are performed to sulfate the catalyst. These simulations mimic the conditions in the aftertreatment system, where periodic regeneration is applied to extend the catalyst lifetime. The catalyst is first sulfated under NH_3-SCR conditions with 30 ppm SO_2, followed by regeneration, and this cycle is repeated ten times. Three different temperatures are investigated for the regeneration and the results are shown in Figure 6.5(b).
The results denoted *Sulfated* corresponds to the deactivation just after SO_2 exposure, and the result denoted *Regenerated* corresponds to the deactivation after the thermal regeneration. For both cases, the deacivation increases as a function of cycle. Comparing the *Sulfated* deactivation with the *Regenerated* deactivation, it is clear that the catalyst does regain some of the activity after regeneration, however the deactivation still increases over time. A higher regeneration temperature results in a lower deactivation. Integration of the sulfur release during regeneration shows a higher amount when heating to 450 °C compared to 400 °C as would be expected. Since sulfation is always carried out under identical conditions, this suggests that

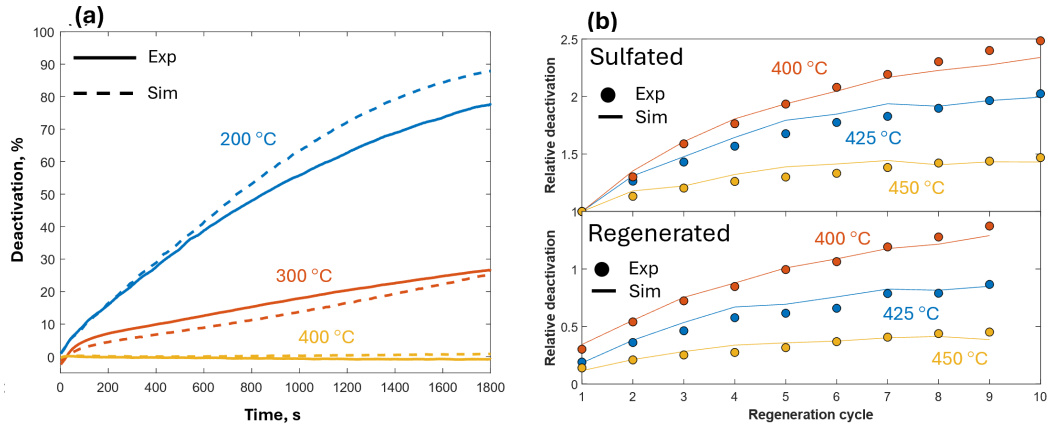

Figure 6.5: (a): Deactivation for sulfation experiments with 30 ppm SO_2 in NH_3-SCR conditions at 200, 300 and 400 °C. (b) Relative deactivation for sulfation-regeneration experiments for after sulfation (*Sulfated*) and after regeneration (*Regenerated*). The regeneration is performed up to 400, 425 and 450 °C. Sulfation is done at 200 °C. The relative deactivation is the deactivation divided by the deactivation of the sulfated state after the first cycle.

a larger amount of SO_2 remains on the catalyst after regeneration at 400 °C. The model can describe the trend in the deactivation for the different temperatures.
To better understand the interplay between $S_1-HSO_4NH_4$ and S_2-HSO_4, the evolution of sulfur coverage is investigated in Figure 6.6. Figure 6.6(a) displays the experimental NO concentration and temperature with the sulfation periods highlighted in yellow for 4 cycles. As SO_2 is dosed, the NO conversion drops rapidly. Figure 6.6(b) shows the evolution of the coverage and SO_2 release predicted by the model following the protocol in Figure 6.6(a). During the sulfation, only $S_1-HSO_4NH_4$ is formed. As the temperature increases, $S_1-HSO_4NH_4$ is either decomposed as SO_2 or transformed into S_2-HSO_4. The fact that S_2-HSO_4 is only formed during the regeneration highlights the importance of optimizing the regeneration conditions to prevent transformation to S_2-HSO_4. The interplay between $S_1-HSO_4NH_4$ and S_2-HSO_4 in the model provides a handle for optimizing the sulfur tolerance of the catalyst.

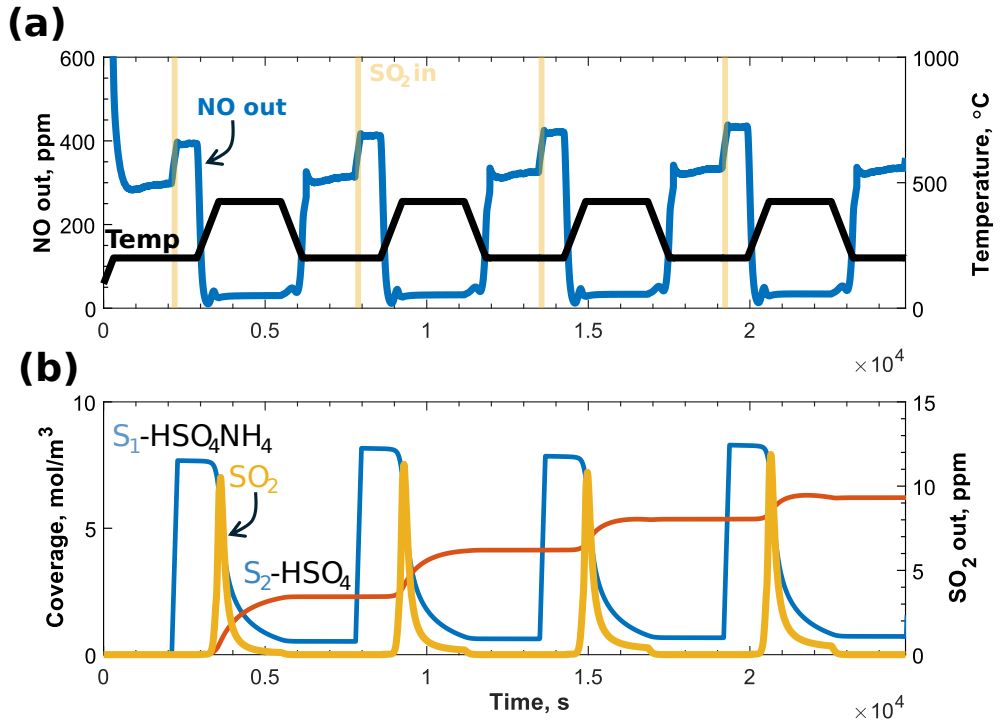

Figure 6.6: Sulfation regeneration procedure of four cycles. (a): Experimental NO out and temperature. A yellow color is used to highlight when SO_2 is dosed (b): The evolution of the coverage and SO_2 release predicted by the model, following the experiments in (a).

7

Conclusions and Outlook

This thesis investigates the dynamics and reactivity of the Cu species in Cu-CHA, as well as the influence of sulfur species for NH_3-SCR, using a combination of theoretical and experimental methods. Cu ions are dynamic in the sense they can have different speciations depending on reaction conditions. First principle-based micro-kinetic modeling is used to study H_2-TPR profiles, which can be used to distingiush between different Cu species. To study the diffusion of Cu ions in the zeolite, a machine learning force field was constructed to enable simulations of larger systems over extended times, which was necessary to capture the diffusion dynamics. DFT calculations, experiments and kinetic modelling is used to study sulfur poisoning of NH_3-SCR.

H_2-TPR is a common technique to characterize the Cu ions in Cu-CHA, however, the interpretation is often ambiguous. To understand which Cu ions may be influencing the H_2-TPR profiles, a first-principle-based micro-kinetic model was developed. Several Cu sites in oxidation state +2 consumed H_2, which was Z_2CuOCu, ZCuOH, $Z_2CuHOOHCu$, Z_2Cu and $Z_2CuOOCu$. The micro-kinetic model agreed well with the experimental findings and provided a way to link specific Cu sites to the reduction temperatures.

A machine learning force-field was constructed to study the mobility and pairing of $[Cu(NH_3)_2]^+$ complexes. Metadynamics simulations revealed that the presence of neighboriing $[Cu(NH_3)_2]^+$ and $NH_4{}^+$ cations affects each other's movements. By varying the zeolite composition, it was found that the fraction of paired $[Cu(NH_3)_2]^+$ complexes is enhanced by increasing the Cu/Al ratio and decreasing the Si/Al ratio. Interestingly, for a high amount of Al and $NH_4{}^+$ ions, the simulated fraction of paired $[Cu(NH_3)_2]^+$ complexes is higher than if they were distribution randomly. Lastly, the lifetime of the pairs vary significantly, highlighting the heterogeneous nature of Cu-CHA, where some configuration are more stable than others. Machine learning force-field provides information on the diffusion dynamics of $[Cu(NH_3)_2]^+$ and the interplay between the Al ions and counter ions otherwise inaccessible to conventional AIMD simulations.

The reactivity of sulfur towards Cu ions during both and high-temperature NH_3-SCR conditions was studied using DFT calculations. At low temperature, SO_2 was found to react strongly with the peroxo complex $[Cu_2(NH_3)_4O_2]^{2+}$. With this result, a reaction mechanism was proposed involving the reaction of SO_2, NO, and NH_3, to form H_2SO_4, H_2O and N_2. As H_2SO_4 is a bulky molecule it may accumulate in the cage over time deactivating the catalyst. H_2SO_4 can interact with other NH_3 species and a thermodynamic analysis was performed that found the $HSO_4(NH_4)$

species to be most stable at typical reaction conditions. Lastly, AIMD simulations suggested that the presence of two $HSO_4(NH_4)$ species destabilizes the pairing of $[Cu(NH_3)_2]^+$, inhibiting the adsorption of O_2. The reaction of SO_2 and SO_3 towards the framework-bound Cu complexes Z_2Cu, ZCuOH and ZCuOOCu present at high temperature, showed that more stable Cu sulfates were formed when reacting with SO_3. ZCuOH and ZCuOOCu form more stable Cu sulfur complexes compared to Z_2Cu. The two studies show that there is a large difference in the poisoning mechanism depending the temperature. At low temperatures, the poisoning mechanism is physical blocking by the accumulation of $HSO_4(NH_4)$ species, while at high temperatures, the Cu sites are blocked by forming stable Cu sulfites/sulfates.

Based on the previous findings from DFT calculations, a kinetic model was developed and parameterized to reactor flow experiments. The model consist of two sites $S_1-HSO_4NH_4$ and S_2-HSO_4, which describe reversible and irreversible deactivation, respectively. Sulfation regeneration experiments showed that while the regeneration procedure recovers part of the lost activity, deactivation still increases with each cycle. The irreversible deactivation (S_2-HSO_4) only forms during the regeneration, which shows the importance of optimizing the regeneration conditions to minimize long-term deactivation. The interplay between reversible deactivation ($S_1-HSO_4NH_4$) and irreversible deactivation (S_2-HSO_4) provides a framework to improve regeneration by limiting the formation of S_2-HSO_4.

Although the use of ML-FF can provide new insights not accessible by standard DFT, the method also has limitations. The ML-FF can be challenging to validate against experimental data, and is instead typically validated against DFT calculations. However, since the ML-FF is trained on DFT data, it inherits the same limitation, such as the approximation of the exchange-correlation term. In addition, DFT calculations of the large systems used in ML-FF simulations is not feasible, thus, the ML-FF can only be validated on smaller systems. The use of machine learning force-fields allows simulation in the range of microseconds, however, turnover frequencies typically occur at much longer timescales. To extend simulation times, a kinetic Monte Carlo model can be used, in which the rates may be calculated from the machine learning force-field.

The low-temperature sulfur deactivation is linked to the destabilization of paired $[Cu(NH_3)_2]^+$ complexes, however, this has only been studied using small unit cells with short simulation times. To study how $HSO_4(NH_4)$ species influence the pairing of $[Cu(NH_3)_2]^+$ complexes, the machine learning force-field constructed in this thesis could be extended to allow simulations containing sulfur species, or a kMC model including sulfur species could be constructed. The kinetic model constructed for sulfur poisoning demonstrates the potential for optimizing the regeneration procedure. Studying how the gas composition, flow rate, and other factors affect the deSO_x efficiency could provide valuable insights needed for extending the lifetime of the catalyst. Under practical conditions, NO_2 is also present, and the SO_x induced deactivation of the fast SCR reaction should be investigated.

The thesis combines theoretical and experimental techniques to give a comprehensive understanding of the NH_3-SCR mechanism over Cu-CHA, and the deactivation

caused by SO_2. By incorporating findings from first-principles calculations into reactor models, it is possible to connect observations from atomistic insights with experimental observations under realistic conditions. The emergence of ML-FF as a new approach in the computational toolbox opens the possibility to simulate larger systems over longer timescales, allowing the study of Cu dynamics under conditions closer to real catalytic operation. Overall, the findings and workflow presented here help bridge the gap between theory and experiment and can guide the development of more active catalysts.

Acknowledgements

The research was carried out at the Division of Chemical Physics and Competence Centre for Catalysis at Chalmers University of Technology, Göteborg, Sweden, and at Umicore AG & Co. KG, Hanau, Germany in the period October 2021 to October 2025.

The research was funded by the European Union's Horizon 2020 research and innovation programme under the Marie Sklodowska-Curie grant agreement no. 955839 (CHASS), with additional support from the Swedish Energy Agency (52689-1).

The Competence Centre for Catalysis is hosted by Chalmers University of Technology, and financially supported by the Swedish Energy Agency, and the member companies: Johnson Matthey, Perstorp, Preem, Powercell, Scania CV, Umicore, and Volvo Group

Computational time was granted by NAISS at C3SE (Göteborg), PDC (Stockholm) and NSC (Linköping).

In addition, I want to thank:

My main supervisor, Henrik Grönbeck. Thank you for your guidance, support, and encouragement throughout my PhD. Working with you has been an inspiring and rewarding experience.

My co-supervisor Martin Votsmeier, for the many valuable discussions and for your helpful advice on my research.

Riccardo Uglietti for introducing me to the world of chemical engineering and for the endless hours of guidance, help, and stimulating discussions.

The members of the CHASS project for the valuable discussions and ideas. It has always been a pleasure to attend our project meetings.

All colleagues at both Chemical Physics and Umicore, for creating a supportive and enjoyable working environment.

Lastly, I would like to thank my family and friends for always supporting me and for encouraging me to pursue my interests.

Bibliography

1. Collins, W. D., Ramaswamy, V., Schwarzkopf, M. D., Sun, Y., Portmann, R. W., Fu, Q., Casanova, S. E. B., Dufresne, J.-L., Fillmore, D. W., Forster, P. M. D., Galin, V. Y., Gohar, L. K., Ingram, W. J., Kratz, D. P., Lefebvre, M.-P., Li, J., Marquet, P., Oinas, V., Tsushima, Y., Uchiyama, T. & Zhong, W. Y. Radiative Forcing by Well-Mixed Greenhouse Gases: Estimates from Climate Models in the Intergovernmental Panel on Climate Change (IPCC) Fourth Assessment Report (AR4). *J. Geophys. Res.: Atmos.* **111** (2006).
2. Health organization, W. WHO Global air quality guidelines. Particulate matter ($PM_{2.5}$ and PM_{10}), ozone, nitrogen oxide, sulfur dioxide and carbon monoxide. (ed Organization, W. H.) (2021).
3. Health Effects Institute. *State of Global Air 2024. Special Report* tech. rep. (Health Effects Institute, Boston, MA, 2024).
4. Skalska, K., Miller, J. S. & Ledakowicz, S. Trends in NO Abatement: A Review. *Sci. Total Environ.* **408,** 3976–3989 (2010).
5. European Environment Agency. *Air Quality in Europe: 2019 Report.* (Publications Office, LU, 2019).
6. Selleri, T., Melas, A. D., Joshi, A., Manara, D., Perujo, A. & Suarez-Bertoa, R. An Overview of Lean Exhaust deNO_x Aftertreatment Technologies and NO_x Emission Regulations in the European Union. *Catal.* **11,** 404 (2021).
7. International Union of Pure and Applied Chemistry (IUPAC) (2019).
8. Bertini, I. *Inorganic and Bio-Inorganic Chemistry - Volume II* (2009).
9. Heveling, J. Heterogeneous Catalytic Chemistry by Example of Industrial Applications. *J. Chem. Educ.* **89,** 1530–1536 (2012).
10. Argyle, M. D. & Bartholomew, C. H. Heterogeneous Catalyst Deactivation and Regeneration: A Review. *Catal.* **5,** 145–269 (2015).
11. Atkinson, R. Atmospheric Chemistry of VOCs and NOV. *Atmospheric Environment* (2000).
12. Abbasi, T., Poornima, P., Kannadasan, T. & Abbasi, S. Acid Rain: Past, Present, and Future. *Int. J. Environ. Eng.* **5,** 229–272 (2013).
13. Hasager, F., Bjerregaard, J. D., Bonomaully, J., Knap, H., Afshari, A. & Johnson, M. S. in *Air Pollution Sources, Statistics and Health Effects* 135–162 (Springer US, 2021).
14. Wang, J., Chen, H., Hu, Z., Yao, M. & Li, Y. A Review on the Pd-Based Three-Way Catalyst. *Catal. Rev.* **57,** 79–144 (2015).
15. Miyoshi, N., Matsumoto, S., Katoh, K., Tanaka, T., Harada, J., Takahashi, N., Yokota, K., Sugiura, M. & Kasahara, K. Development of New Concept

Three-Way Catalyst for Automotive Lean-Burn Engines. *SAE trans.* **104,** 1361–1370 (1995).
16. Wang, A. & Olsson, L. The impact of automotive catalysis on the United Nations sustainable development goals. *Nat. Catal.,* 566–570 (2019).
17. Russell, A. & Epling, W. S. Diesel Oxidation Catalysts. *Catal. Rev.* **53,** 337–423 (2011).
18. Forster, P. M. F. *et al.* in *Climate Change 2021: The Physical Science Basis. Contribution of Working Group I to the Sixth Assessment Report of the Intergovernmental Panel on Climate Change* (Cambridge University Press, 2021).
19. Damma, D., Ettireddy, P. R., Reddy, B. M. & Smirniotis, P. G. A Review of Low Temperature NH_3-SCR for Removal of NO_x. *Catal.* **9,** 349 (2019).
20. Zhang, J., Li, X., Chen, P. & Zhu, B. Research Status and Prospect on Vanadium-Based Catalysts for NH_3-SCR Denitration. *Materials* **11,** 1632 (2018).
21. Chen, H., Xia, Y., Fang, R., Huang, H., Gan, Y., Liang, C., Zhang, J., Zhang, W. & Liu, X. The Effects of Tungsten and Hydrothermal Aging in Promoting NH_3-SCR Activity on V_2O_5/WO_3-TiO_2 Catalysts. *Appl. Surf. Sci.* **459,** 639–646 (2018).
22. Schildhauer, T. J., Elsener, M., Moser, J., Begsteiger, I., Chatterjee, D., Rusch, K. & Kröcher, O. Measurement of Vanadium Emissions from SCR Catalysts by ICP-OES: Method Development and First Results. *Emiss. Control Sci. Technol.* **1,** 292–297 (2015).
23. Davis, M. E. & Lobo, R. F. Zeolite and Molecular Sieve Synthesis. *Chem. Mater.* **4,** 756–768 (1992).
24. Xin, Y., Li, Q. & Zhang, Z. Zeolitic Materials for $DeNO_x$ Selective Catalytic Reduction. *ChemCatChem* **10,** 29–41 (2018).
25. *IZA Structure Commission* `http://www.iza-structure.org/` (2024).
26. Luo, J.-Y., Oh, H., Henry, C. & Epling, W. Effect of C_3H_6 on Selective Catalytic Reduction of NOx by NH_3 over a Cu/Zeolite Catalyst: A Mechanistic Study. *Appl. Catal. B* **123–124,** 296–305 (2012).
27. Wilken, N., Wijayanti, K., Kamasamudram, K., Currier, N. W., Vedaiyan, R., Yezerets, A. & Olsson, L. Mechanistic Investigation of Hydrothermal Aging of Cu-Beta for Ammonia SCR. *Appl. Catal. B* **111,** 58–66 (2011).
28. Auvray, X., Arvanitidou, M., Högström, Å., Jansson, J., Fouladvand, S. & Olsson, L. Comparative Study of SO_2 and SO_2/SO_3 Poisoning and Regeneration of Cu/BEA and Cu/SSZ-13 for NH_3 SCR. *Emiss. Control Sci. Technol.* **7,** 232–246 (2021).
29. Schmieg, S. J., Oh, S. H., Kim, C. H., Brown, D. B., Lee, J. H., Peden, C. H. F. & Kim, D. H. Thermal Durability of Cu-CHA NH_3-SCR Catalysts for Diesel NOx Reduction. *Catal. Today* **184,** 252–261 (2012).
30. Kwak, J. H., Tonkyn, R. G., Kim, D. H., Szanyi, J. & Peden, C. H. F. Excellent Activity and Selectivity of Cu-SSZ-13 in the Selective Catalytic Reduction of NOx with NH_3. *J. Catal.* **275,** 187–190 (2010).
31. Paolucci, C., Khurana, I., Parekh, A. A., Li, S., Shih, A. J., Li, H., Di Iorio, J. R., Albarracin-Caballero, J. D., Yezerets, A., Miller, J. T., Delgass, W. N.,

Ribeiro, F. H., Schneider, W. F. & Gounder, R. Dynamic Multinuclear Sites Formed by Mobilized Copper Ions in NOx Selective Catalytic Reduction. *Science* **357,** 898–903 (2017).

32. Chen, L., Janssens, T. V. W., Vennestrøm, P. N. R., Jansson, J., Skoglundh, M. & Grönbeck, H. A Complete Multisite Reaction Mechanism for Low-Temperature NH_3-SCR over Cu-CHA. *ACS Catal.* **10,** 5646–5656 (2020).
33. Feng, Y., Wang, X., Janssens, T. V. W., Vennestrøm, P. N. R., Jansson, J., Skoglundh, M. & Grönbeck, H. First-Principles Microkinetic Model for Low-Temperature NH_3-Assisted Selective Catalytic Reduction of NO over Cu-CHA. *ACS Catal.* **11,** 14395–14407 (2021).
34. Feng, Y., Janssens, T. V. W., Vennestrøm, P. N. R., Jansson, J., Skoglundh, M. & Grönbeck, H. High-Temperature Reaction Mechanism of NH3-SCR over Cu-CHA: One or Two Copper Ions? *J. Phys. Chem. C.* **128** (2024).
35. Shan, Y., Du, J., Zhang, Y., Shan, W., Shi, X., Yu, Y., Zhang, R., Meng, X., Xiao, F.-S. & He, H. Selective Catalytic Reduction of NO_x with NH_3: Opportunities and Challenges of Cu-based Small-Pore Zeolites. *Natl. Sci. Rev.* **8,** nwab010 (2021).
36. Gao, F. & Szanyi, J. On the Hydrothermal Stability of Cu/SSZ-13 SCR Catalysts. *Appl. Catal. A Gen.* **560,** 185–194 (2018).
37. Hammershøi, P. S., Jensen, A. D. & Janssens, T. V. W. Impact of SO_2-poisoning over the Lifetime of a Cu-CHA Catalyst for NH_3-SCR. *Appl. Catal. B* **238,** 104–110 (2018).
38. Hammershøi, P. S., Jangjou, Y., Epling, W. S., Jensen, A. D. & Janssens, T. V. W. Reversible and Irreversible Deactivation of Cu-CHA NH_3-SCR catalysts by SO_2 and SO_3. *Appl. Catal. B* **226,** 38–45 (2018).
39. Jangjou, Y., Do, Q., Gu, Y., Lim, L.-G., Sun, H., Wang, D., Kumar, A., Li, J., Grabow, L. C. & Epling, W. S. Nature of Cu Active Centers in Cu-SSZ-13 and Their Responses to SO_2 Exposure. *ACS Catal.* **8,** 1325–1337 (2018).
40. Bjerregaard, J. D., Votsmeier, M. & Grönbeck, H. Mechanism for SO_2 Poisoning of Cu-CHA during Low Temperature NH_3-SCR. *J. Catal.* **417,** 497–506 (2023).
41. Cheng, Y., Montreuil, C., Cavataio, G. & Lambert, C. Sulfur Tolerance and $DeSO_x$ Studies on Diesel SCR Catalysts. *SAE Int. J. Fuels Lubr.* **1,** 471–476 (2008).
42. Jia, L., Liu, J., Huang, D., Zhao, J., Zhang, J., Li, K., Li, Z., Zhu, W., Zhao, Z. & Liu, J. Interface Engineering of a Bifunctional Cu-SSZ-13@CZO Core–Shell Catalyst for Boosting Potassium Ion and SO_2 Tolerance. *ACS Catal.* **18,** 11281–11293 (2022).
43. Paolucci, C., Parekh, A. A., Khurana, I., Di Iorio, J. R., Li, H., Albarracin Caballero, J. D., Shih, A. J., Anggara, T., Delgass, W. N., Miller, J. T., Ribeiro, F. H., Gounder, R. & Schneider, W. F. Catalysis in a Cage: Condition-Dependent Speciation and Dynamics of Exchanged Cu Cations in SSZ-13 Zeolites. *J. Am. Chem. Soc.* **138,** 6028–6048 (2016).
44. Bjerregaard, J. *Dynamics and Reactivity of Cu-species in Cu-CHA for NH_3-SCR* Licentiate thesis (Chalmers University of Technology, Gothenburg, Sweden, 2024).

45. Hartree, D. R. The Wave Mechanics of an Atom with a Non-Coulomb Central Field. Part II. Some Results and Discussion. *Math. Proc. Cambridge Philos. Soc.* **24,** 111–132 (1928).
46. Fock, V. Näherungsmethode zur Lösung des quantenmechanischen Mehrkörperproblems. *Zeitschrift für Physik* **61,** 126–148 (1930).
47. Hohenberg, P. & Kohn, W. Inhomogeneous Electron Gas. *Phys. Rev.* **136,** B864–B871 (1964).
48. Kohn, W. & Sham, L. J. Self-Consistent Equations Including Exchange and Correlation Effects. *Phys. Rev.* **140,** A1133–A1138 (1965).
49. Ceperley, D. M. & Alder, B. J. Ground State of the Electron Gas by a Stochastic Method. *Phys. Rev. Lett.* **45,** 566–569 (1980).
50. Cohen, A. J., Mori-Sánchez, P. & Yang, W. Challenges for Density Functional Theory. *Chem. Rev.,* 289–320 (2012).
51. Perdew, J. P., Burke, K. & Ernzerhof, M. Generalized Gradient Approximation Made Simple. *Phys. Rev. Lett.* **77,** 3865–3868 (1996).
52. Jensen, F. *Introduction to Computational Chemistry* 3rd. 638 pp. ISBN: 978-1-118-82599-0 (Wiley, 2017).
53. Becke, A. D. A New Mixing of Hartree–Fock and Local Density-functional Theories. *J. Chem. Phys.* **98,** 1372–1377 (1993).
54. Lee, C., Yang, W. & Parr, R. G. Development of the Colle-Salvetti Correlation-Energy Formula into a Functional of the Electron Density. *Phys. Rev. B* **37,** 785–789 (1988).
55. Dudarev, S. L., Botton, G. A., Savrasov, S. Y., Humphreys, C. J. & Sutton, A. P. Electron-Energy-Loss Spectra and the Structural Stability of Nickel Oxide: An LSDA+U Study. *Phys. Rev. B* **57,** 1505–1509 (1998).
56. Arovas, D. P., Berg, E., Kivelson, S. A. & Raghu, S. The Hubbard Model. *Annu. Rev. Condens. Matter Phys.* **13,** 239–274 (2022).
57. Dion, M., Rydberg, H., Schröder, E., Langreth, D. C. & Lundqvist, B. I. Van Der Waals Density Functional for General Geometries. *Phys. Rev. Lett.* **92,** 246401 (2004).
58. Grimme, S., Antony, J., Ehrlich, S. & Krieg, H. A Consistent and Accurate Ab Initio Parametrization of Density Functional Dispersion Correction (DFT-D) for the 94 Elements H-Pu. *J. Chem. Phys.* **132,** 154104 (2010).
59. Kohanoff, J. *Electronic Structure Calculations for Solids and Molecules Theory and Computational Methods* ISBN: 9780511755613 (Cambridge University Press, 2006).
60. Blöchl, P. E. Projector Augmented-Wave Method. *Phys. Rev. B* **50,** 17953–17979 (1994).
61. Tang, W., Sanville, E. & Henkelman, G. A Grid-Based Bader Analysis Algorithm without Lattice Bias. *J. Phys.: Condens. Matter* **21,** 084204 (2009).
62. Yu, M. & Trinkle, D. R. Accurate and Efficient Algorithm for Bader Charge Integration. *J. Chem. Phys.* **134,** 064111 (2011).
63. Ponder, J. W. & Case, D. A. in *Advances in Protein Chemistry* 27–85 (2003).
64. Krieger, E., Darden, T., Nabuurs, S. B., Finkelstein, A. & Vriend, G. Making Optimal Use of Empirical Energy Functions: Force-field Parameterization in Crystal Space. *Proteins Struct. Funct. Bioinf.* **57,** 678–683 (2004).

65. Case, D. A., Cheatham III, T. E., Darden, T., Gohlke, H., Luo, R., Merz Jr., K. M., Onufriev, A., Simmerling, C., Wang, B. & Woods, R. J. The Amber Biomolecular Simulation Programs. *J. Comput. Chem.* **26,** 1668–1688 (2005).
66. Rappe, A. K., Casewit, C. J., Colwell, K. S., Goddard, W. A. I. & Skiff, W. M. UFF, a Full Periodic Table Force Field for Molecular Mechanics and Molecular Dynamics Simulations. *J. Am. Chem. Soc.* **114,** 10024–10035 (1992).
67. Unke, O. T., Chmiela, S., Sauceda, H. E., Gastegger, M., Poltavsky, I., Schütt, K. T., Tkatchenko, A. & Müller, K.-R. Machine Learning Force Fields. *Chem. Rev.* **121,** 10142–10186 (2021).
68. Van Duin, A. C. T., Dasgupta, S., Lorant, F. & Goddard, W. A. ReaxFF: A Reactive Force Field for Hydrocarbons. *J. Phys. Chem. A* **105,** 9396–9409 (2001).
69. Senftle, T. P., Hong, S., Islam, M. M., Kylasa, S. B., Zheng, Y., Shin, Y. K., Junkermeier, C., Engel-Herbert, R., Janik, M. J., Aktulga, H. M., Verstraelen, T., Grama, A. & van Duin, A. C. T. The ReaxFF Reactive Force-Field: Development, Applications and Future Directions. *npj Comput. Mater.* **2,** 1–14 (2016).
70. Anstine, D. M. & Isayev, O. Machine Learning Interatomic Potentials and Long-Range Physics. *J. Phys. Chem. A* **127,** 2417–2431 (2023).
71. Zhang, L., Wang, H., Muniz, M. C., Panagiotopoulos, A. Z., Car, R. & E, W. A Deep Potential Model with Long-Range Electrostatic Interactions. *J. Chem. Phys.* **156,** 124107 (2022).
72. Zhang, L., Han, J., Wang, H., Car, R. & E, W. Deep Potential Molecular Dynamics: A Scalable Model with the Accuracy of Quantum Mechanics. *Phys. Rev. Lett.* **120,** 143001 (2018).
73. Keith, J. A., Vassilev-Galindo, V., Cheng, B., Chmiela, S., Gastegger, M., Müller, K.-R. & Tkatchenko, A. Combining Machine Learning and Computational Chemistry for Predictive Insights Into Chemical Systems. *Chem. Rev.* **121,** 9816–9872 (2021).
74. Henkelman, G. & Jónsson, H. Improved Tangent Estimate in the Nudged Elastic Band Method for Finding Minimum Energy Paths and Saddle Points. *J. Chem. Phys.* **113,** 9978–9985 (2000).
75. Henkelman, G., Uberuaga, B. P. & Jónsson, H. A Climbing Image Nudged Elastic Band Method for Finding Saddle Points and Minimum Energy Paths. *J. Chem. Phys.* **113,** 9901–9904 (2000).
76. Lucas, K. *Applied Statistical Thermodynamics* 529 pp. ISBN: 978-3-662-01648-0 (Springer Science & Business Media, 2013).
77. Jørgensen, M., Chen, L. & Grönbeck, H. Monte Carlo Potential Energy Sampling for Molecular Entropy in Zeolites. *J. Phys. Chem. C* **122,** 20351–20357 (2018).
78. Swope, W. C., Andersen, H. C., Berens, P. H. & Wilson, K. R. A Computer Simulation Method for the Calculation of Equilibrium Constants for the Formation of Physical Clusters of Molecules: Application to Small Water Clusters. *J. Chem. Phys.* **76,** 637–649 (1982).
79. Kühne, T. D. Second Generation Car–Parrinello Molecular Dynamics. *WIREs. Comput. Mol. Sci.,* 391–406 (2014).

80. Nosé, S. A Unified Formulation of the Constant Temperature Molecular Dynamics Methods. *J. Chem. Phys.* **81,** 511–519 (1984).
81. Hoover, W. G. Canonical Dynamics: Equilibrium Phase-Space Distributions. *Phys. Rev. A* **31,** 1695–1697 (1985).
82. Frenkel, D. & Smit, B. *Understanding Molecular Simulation: From Algorithms to Applications* ISBN: 978-0-12-267351-1 (Academic Press, 2002).
83. Christ, C. D., Mark, A. E. & van Gunsteren, W. F. Basic Ingredients of Free Energy Calculations: A Review. *J. Comput. Chem.,* 1569–1582 (2010).
84. Branduardi, D., Gervasio, F. L. & Parrinello, M. From A to B in Free Energy Space. *J. Chem. Phys.* **126,** 054103 (2007).
85. Woo, T. K., Margl, P. M., Blöchl, P. E. & Ziegler, T. A Combined Car Parrinello QM/MM Implementation for Ab Initio Molecular Dynamics Simulations of Extended Systems: Application to Transition Metal Catalysis. *J. Phys. Chem. B* **101,** 7877–7880 (1997).
86. Barducci, A., Bussi, G. & Parrinello, M. Well-Tempered Metadynamics: A Smoothly Converging and Tunable Free-Energy Method. *Phys. Rev. Lett.* **100,** 020603 (2008).
87. Carter, E. A., Ciccotti, G., Hynes, J. T. & Kapral, R. Constrained Reaction Coordinate Dynamics for the Simulation of Rare Events. *Phys. Rev. Lett.* **156,** 472–477 (1989).
88. Laio, A. & Parrinello, M. Escaping Free-Energy Minima. *Proc. Natl. Acad. Sci.* **99,** 12562–12566 (2002).
89. Sutto, L., Marsili, S. & Gervasio, F. L. New Advances in Metadynamics. *WIREs Comput. Mol. Sci.* **2,** 771–779 (2012).
90. Raiteri, P., Laio, A., Gervasio, F. L., Micheletti, C. & Parrinello, M. Efficient Reconstruction of Complex Free Energy Landscapes by Multiple Walkers Metadynamics. *J. Phys. Chem. B* **110,** 3533–3539 (2006).
91. Chorkendorff, I. & Niemantsverdriet, J. W. *Concepts of Modern Catalysis and Kinetics* ISBN: 3-527-30574-2 (WILEY, 2003).
92. Fogler, H. S. *Elements of Chemical Reaction Engineering* ISBN: 0-13-047394-4 (Prentince Hall, 2006).
93. Motagamwala, A. H. & Dumesic, J. A. Microkinetic Modeling: A Tool for Rational Catalyst Design. *Chem. Rev.* **121,** 1049–1076 (2021).
94. Han, J., Wang, A., Isapour, G., Härelind, H., Skoglundh, M., Creaser, D. & Olsson, L. N_2O Formation during NH_3-SCR over Different Zeolite Frameworks: Effect of Framework Structure, Copper Species, and Water. *Ind. Eng. Chem. Res.* **60,** 17826–17839 (2021).
95. Molokova, A. Y., Borfecchia, E., Martini, A., Pankin, I. A., Atzori, C., Mathon, O., Bordiga, S., Wen, F., Vennestrøm, P. N. R., Berlier, G., Janssens, T. V. W. & Lomachenko, K. A. SO_2 Poisoning of Cu-CHA deNO_x Catalyst: The Most Vulnerable Cu Species Identified by X-ray Absorption Spectroscopy. *JACS Au* (2022).
96. Chen, L., Jansson, J., Skoglundh, M. & Grönbeck, H. Mechanism for Solid-State Ion Exchange of Cu^+ into Zeolites. *The Journal of Physical Chemistry C* **120,** 29182–29189 (2016).

97. Zhang, Y., Peng, Y., Li, J., Groden, K., McEwen, J.-S., Walter, E. D., Chen, Y., Wang, Y. & Gao, F. Probing Active-Site Relocation in Cu/SSZ-13 SCR Catalysts during Hydrothermal Aging by In Situ EPR Spectroscopy, Kinetics Studies, and DFT Calculations. *ACS Catal.* **10,** 9410–9419 (2020).
98. Gao, F., Washton, N. M., Wang, Y., Kollár, M., Szanyi, J. & Peden, C. H. F. Effects of Si/Al Ratio on Cu/SSZ-13 NH_3-SCR Catalysts: Implications for the Active Cu Species and the Roles of Brønsted Acidity. *J. Catal.* **331,** 25–38 (2015).
99. Gao, F., Walter, E. D., Karp, E. M., Luo, J., Tonkyn, R. G., Kwak, J. H., Szanyi, J. & Peden, C. H. F. Structure–Activity Relationships in NH_3-SCR over Cu-SSZ-13 as Probed by Reaction Kinetics and EPR Studies. *J. Catal.* **300,** 20–29 (2013).
100. Nielsen, D., Gao, Q., Janssens, T. V. W., Vennestrøm, P. N. R. & Mossin, S. Cu-Speciation in Dehydrated CHA Zeolites Studied by H_2-TPR and In Situ EPR. *J. Phys. Chem. C* **127,** 12995–13004 (2023).
101. Kwak, J. H., Zhu, H., Lee, J. H., Peden, C. H. F. & Szanyi, J. Two Different Cationic Positions in Cu-SSZ-13? *Chem. Commun.* **48,** 4758–4760 (2012).
102. Ipek, B., Wulfers, M. J., Kim, H., Göltl, F., Hermans, I., Smith, J. P., Booksh, K. S., Brown, C. M. & Lobo, R. F. Formation of $[Cu_2O_2]^{2+}$ and $[Cu_2O]^{2+}$ toward C–H Bond Activation in Cu-SSZ-13 and Cu-SSZ-39. *ACS Catal.* **7,** 4291–4303 (2017).
103. Rhoda, H. M., Plessers, D., Heyer, A. J., Bols, M. L., Schoonheydt, R. A., Sels, B. F. & Solomon, E. I. Spectroscopic Definition of a Highly Reactive Site in Cu-CHA for Selective Methane Oxidation: Tuning a Mono-μ-Oxo Dicopper(II) Active Site for Reactivity. *J. Am. Chem. Soc.* **143,** 7531–7540 (2021).
104. Bregante, D. T., Wilcox, L. N., Liu, C., Paolucci, C., Gounder, R. & Flaherty, D. W. Dioxygen Activation Kinetics over Distinct Cu Site Types in Cu-Chabazite Zeolites. *ACS Catal.* **11,** 11873–11884 (2021).
105. Rizzotto, V., Chen, P. & Simon, U. Mobility of NH_3-Solvated Cu^{II} Ions in Cu-SSZ-13 and Cu-ZSM-5 NH_3-SCR Catalysts: A Comparative Impedance Spectroscopy Study. *Catal.* **8,** 162 (2018).
106. Wu, Y., Ma, Y., Wang, Y., Rappé, K. G., Washton, N. M., Wang, Y., Walter, E. D. & Gao, F. Rate Controlling in Low-Temperature Standard NH_3-SCR: Implications from Operando EPR Spectroscopy and Reaction Kinetics. *J. Am. Chem. Soc.* **144,** 9734–9746 (2022).
107. Millan, R., Cnudde, P., van Speybroeck, V. & Boronat, M. Mobility and Reactivity of Cu^+ Species in Cu-CHA Catalysts under NH_3-SCR-NOx Reaction Conditions: Insights from AIMD Simulations. *JACS Au* **1,** 1778–1787 (2021).
108. Millan, R., Bello-Jurado, E., Moliner, M., Boronat, M. & Gomez-Bombarelli, R. Effect of Framework Composition and NH_3 on the Diffusion of Cu^+ in Cu-CHA Catalysts Predicted by Machine-Learning Accelerated Molecular Dynamics. *ACS Cent. Sci.,* 2044–2056 (2023).
109. Fahami, A. R., Günter, T., Doronkin, D. E., Casapu, M., Zengel, D., Vuong, T. H., Simon, M., Breher, F., Kucherov, A. V., Brückner, A., *et al.* The Dynamic Nature of Cu Sites in Cu-SSZ-13 and the Origin of the Seagull NOx Conversion Profile during NH_3-SCR. *React. Chem. Eng.* **4,** 1000–1018 (2019).

110. Wijayanti, K., Xie, K., Kumar, A., Kamasamudram, K. & Olsson, L. Effect of Gas Compositions on SO_2 Poisoning over Cu/SSZ-13 Used for NH_3-SCR. *Appl. Catal., B* **219,** 142–154 (2017).
111. Xi, Y., Ottinger, N., Su, C. & Liu, Z. G. Sulfur Poisoning of a Cu-SSZ-13 SCR Catalyst under Simulated Diesel Engine Operating Conditions. *SAE Int. J. Adv. Curr. Pract. Mobil.* **3,** 2690–2694 (2021).
112. Mesilov, V., Dahlin, S., Bergman, S. L., Xi, S., Han, J., Olsson, L., Pettersson, L. J. & Bernasek, S. L. Regeneration of Sulfur-Poisoned Cu-SSZ-13 Catalysts: Copper Speciation and Catalytic Performance Evaluation. *Appl. Catal. B* **299,** 120626 (2021).